

JGR Atmospheres

RESEARCH ARTICLE

10.1029/2022JD038394

Key Points:

- The raindrop number predictions of seven double-moment microphysics schemes are evaluated in comparison with disdrometer observations
- The seven schemes show significant biases from the observation and severe discrepancies from each other in the raindrop number prediction
- Disagreements in raindrop number prediction among the schemes mainly originate from different representations of autoconversion and melting

Correspondence to:



J.-J. Baik,
jjbaik@snu.ac.kr

Citation:

Jin, H.-G., & Baik, J.-J. (2023). Do double-moment microphysics schemes make reliable predictions on the raindrop number concentration?: A squall-line case study. *Journal of Geophysical Research: Atmospheres*, 128, e2022JD038394. <https://doi.org/10.1029/2022JD038394>

Received 15 DEC 2022
Accepted 17 APR 2023

Do Double-Moment Microphysics Schemes Make Reliable Predictions on the Raindrop Number Concentration?: A Squall-Line Case Study

Han-Gyul Jin¹  and Jong-Jin Baik¹ 

¹School of Earth and Environmental Sciences, Seoul National University, Seoul, South Korea

Abstract Utilizing raindrop size distribution observations in the evaluation of a cloud microphysics scheme helps identifying systematic deficiencies of the scheme and improving it. In this study, we evaluate the performance of seven different double-moment bulk microphysics schemes in predicting raindrop number concentration N_r in squall-line simulations using ground-based disdrometer observations. While all seven schemes show good performances in the prediction of rainwater mass, they show significant biases from the observation and severe discrepancies from each other in the prediction of N_r . The Thompson, Thompson aerosol-aware, and Weather Research and Forecasting double moment 6-class (WDM6) schemes, where the main source of N_r is melting of snow and graupel, overestimate N_r by four times, which may be caused by overestimation of N_r production via melting. The Morrison and predicted particle properties (P3) schemes, where the autoconversion of cloud droplets into raindrops is an N_r source that is as important as melting, exhibit negative biases of N_r , which may be attributed to insufficient collisional breakup of raindrops. The P3_Nc scheme, the P3 scheme that prognoses cloud droplet number concentration, shows two prominent modes in N_r distribution, one of which consists of overestimated N_r produced by overly active autoconversion. The ice-spheroids habit model with aspect-ratio evolution scheme overestimates N_r but not as much as the two Thompson schemes and WDM6 scheme, showing the most realistic prediction of mean raindrop diameter. The high uncertainty in N_r prediction needs to be reduced by carefully selecting parameterizations for important microphysical processes, in order to maximize the advantage of using double-moment microphysics schemes.

Plain Language Summary The raindrop number concentration is one of the variables predicted by weather models, but the accuracy of the prediction has not been well evaluated. This study evaluates the predictions of raindrop number concentration by seven different cloud models, which gives implications on whether the cloud models reasonably represent the cloud microphysical processes where the raindrop number concentration is involved. For the evaluation, the observation data from a ground-based disdrometer, which measures each raindrop's size and fall speed, are used. In the simulations of a rainfall case, the cloud models all show biased predictions on the raindrop number concentration, in contrast with their predictions on the rain rate, which are all reasonable. In addition, the predictions on the raindrop number concentration by the seven cloud models are severely different from each other. The reason for the severe discrepancies is mainly because the cloud models have substantial disagreements in how they represent the conversion of small droplets into raindrops and the melting of ice particles. To reduce uncertainties in cloud and precipitation predictions, these disagreements among the cloud models should be alleviated.

1. Introduction

Cloud microphysics schemes represent various and complicated physical processes associated with cloud and precipitation particles in a simplified way using parameterizations, playing a crucial role in the prediction of clouds and precipitation, which is a main goal of weather and climate models. One of the biggest challenges in the advance of cloud microphysics schemes is that it is very difficult to evaluate each of the simulated microphysical processes based on cloud and precipitation observations (Morrison et al., 2020). Observed variables such as surface precipitation rate and cloud macrophysical properties have been extensively used to evaluate model performance, but they can provide only limited observational constraints to the cloud microphysical processes in microphysics schemes. In the needs for a further level of evaluation of cloud microphysics in models, some recent studies utilize the observation of drop size distribution characteristics from polarimetric radars, airborne drop size

distribution probes, and ground-based disdrometers (e.g., Brown et al., 2016; Chen et al., 2021; Lei et al., 2020; Lin et al., 2022; Morrison et al., 2022; Wang et al., 2020; Witte et al., 2019; Wu et al., 2021).

Brown et al. (2016) simulated two hurricanes using five different bulk microphysics schemes and one bin microphysics scheme in the Weather Research and Forecasting (WRF) model and evaluated the simulated raindrop size distribution (RSD) characteristics by comparing the observed and simulated polarimetric radar variables. In their cases, the Thompson aerosol-aware scheme (G. Thompson & Eidhammer, 2014) and the “fast” spectral bin microphysics scheme (Lynn et al., 2005) showed the most accurate predictions of radar variables, but even these schemes showed significant discrepancies from the radar observation. Wang et al. (2020) again demonstrated the superior performance of the Thompson aerosol-aware scheme over other bulk schemes in reproducing the radar-retrieved RSD characteristics, in their WRF model simulations of a typhoon. Wu et al. (2021) assessed the RSD prediction performance of three bulk schemes for the convective precipitation in an outer rainband of a typhoon using polarimetric radar observations and showed that the WRF double moment 6-class (WDM6) scheme (Lim & Hong, 2010) underestimates the mean diameter of raindrops, which was attributed to the overly active warm-rain processes in this scheme. In another typhoon case study of Lin et al. (2022), the RSDs simulated using three bulk schemes exhibited overly intense changes while descending to the ground compared to polarimetric radar observations, and they suggested that this may be caused by the inaccurate representation of collision-coalescence process.

The polarimetric radar observation can be a powerful reference for the evaluation of simulated RSD characteristics in that it covers horizontally broad area and provides the information of how RSD characteristics vertically evolve. On the other hand, a weakness of this observation is that the radar-retrieved RSD parameters can be highly uncertain. Lin et al. (2022) reported significant discrepancies between the polarimetric radar-retrieved RSD parameters near the surface and the ground-based disdrometer observation, which were attributed to the uncertainties in the assumptions used for the retrieval such as the slope parameter–shape parameter relationship. According to their Figures 7 and 8, these discrepancies are comparable to the discrepancies in simulated RSD parameters among different schemes. This can be a critical downside of using radar observations to quantitatively estimate the biases in the RSD predictions of microphysics schemes.

In-situ observations such as the ground-based disdrometer and airborne observations enable robust and quantitative evaluation of RSD predictions of microphysics schemes, although the limited coverages are their weakness. From the direct observation of drops, the full drop size distribution in the measurable size range of the instrument is obtained without any assumption so that the prognostic variables in microphysics schemes can be directly compared with their observation counterparts. For example, Lei et al. (2020) evaluated the simulated two prognostic variables (i.e., mass mixing ratios and number concentrations) of cloud droplets and raindrops in the WDM6 scheme in comparison with airborne observations. They found that the WDM6 scheme underestimates the cloud droplet number concentration and overestimates the raindrop number concentration and that these biases originate from inappropriate parameterizations of cloud condensation nuclei activation, cloud droplet evaporation, and melting of snow and graupel. They saw alleviation of biases when they modified those parameterizations in the WDM6 scheme.

As Lei et al. (2020) showed, utilizing RSD observations in the evaluation of a microphysics scheme can give insights into systematic deficiencies in the microphysics scheme and help identifying problematic parameterizations. In this study, we aim to (a) figure out whether double-moment bulk microphysics schemes make reliable predictions of their key prognostic variable, the raindrop number concentration, utilizing ground-based disdrometer observations and (b) identify the microphysics parameterizations that are responsible for the systematic bias in the prediction of raindrop number concentration for each scheme. The main advantage of double-moment microphysics schemes over single-moment microphysics schemes is that they predict the evolution of particle number concentration and use this variable to calculate relevant microphysical processes more accurately (Igels et al., 2015). For example, the gravitational size sorting of raindrops that cannot be represented in single-moment schemes can be represented in double-moment schemes by applying different moment-weighted fall velocities to the sedimentations of mass mixing ratio and number concentration (Milbrandt & McTaggart-Cowan, 2010). The increased degrees of freedom in RSD also enable more realistic representation of rainwater evaporation, which resulted in a successful simulation of widespread trailing stratiform precipitation region of a squall line in Morrison et al. (2009). This kind of advantage of double-moment microphysics schemes will be maximized if the predicted number concentration is close enough to reality. On the other hand, if the predicted number

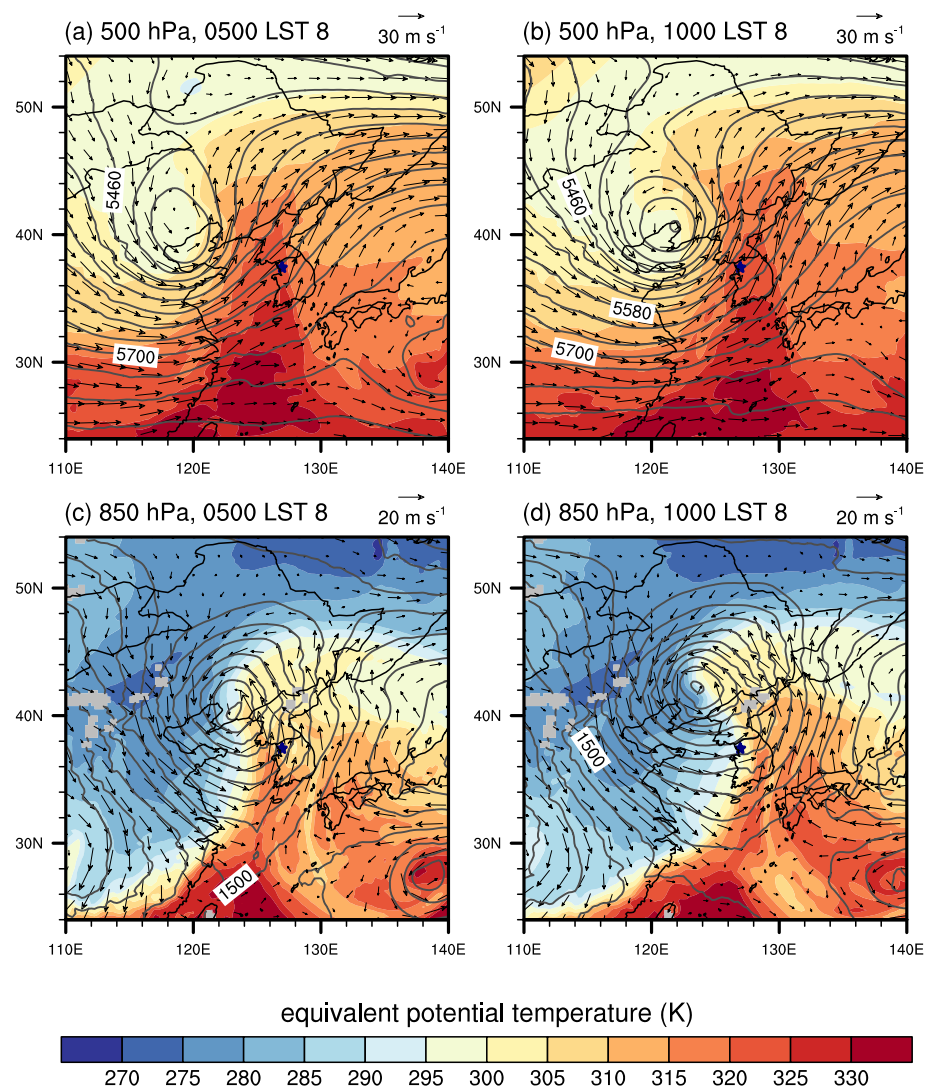


Figure 1. (a, b) 500-hPa and (c, d) 850-hPa fields of geopotential height (gray contours, in 40 m intervals in (a, b) and 20 m intervals in (c, d)), wind vector (arrows), and equivalent potential temperature (color shades) at (a, c) 0500 and (b, d) 1000 LST 8 November 2021. The navy star symbol indicates the location of the disdrometer site in Seoul.

concentration is far from reality, the calculations of microphysical processes where this number concentration is involved will all be problematic.

For the evaluation in this study, a rainfall case associated with a squall line passing South Korea is simulated using a variety of double-moment microphysics schemes in the WRF model. The case description, model configuration, descriptions of the used microphysics schemes, and data descriptions are provided in Section 2. The evaluation results and microphysics analyses are presented in Section 3. A summary and conclusions are given in Section 4.

2. Data and Methods

2.1. Case Description

On 8 November 2021, an eastward-moving squall line aligned in the north–south direction passed Seoul. During 4 hr of its passing (0530–0930 LST), 22 mm of precipitation was accumulated at a rain gauge in Seoul. The squall line was generated ahead of a strong cold front of an extratropical cyclone. Figure 1 shows the 500- and 850-hPa synoptic fields at 0500 and 1000 LST. At 0500 LST, the 500-hPa level trough is located to the west of the 850-hPa

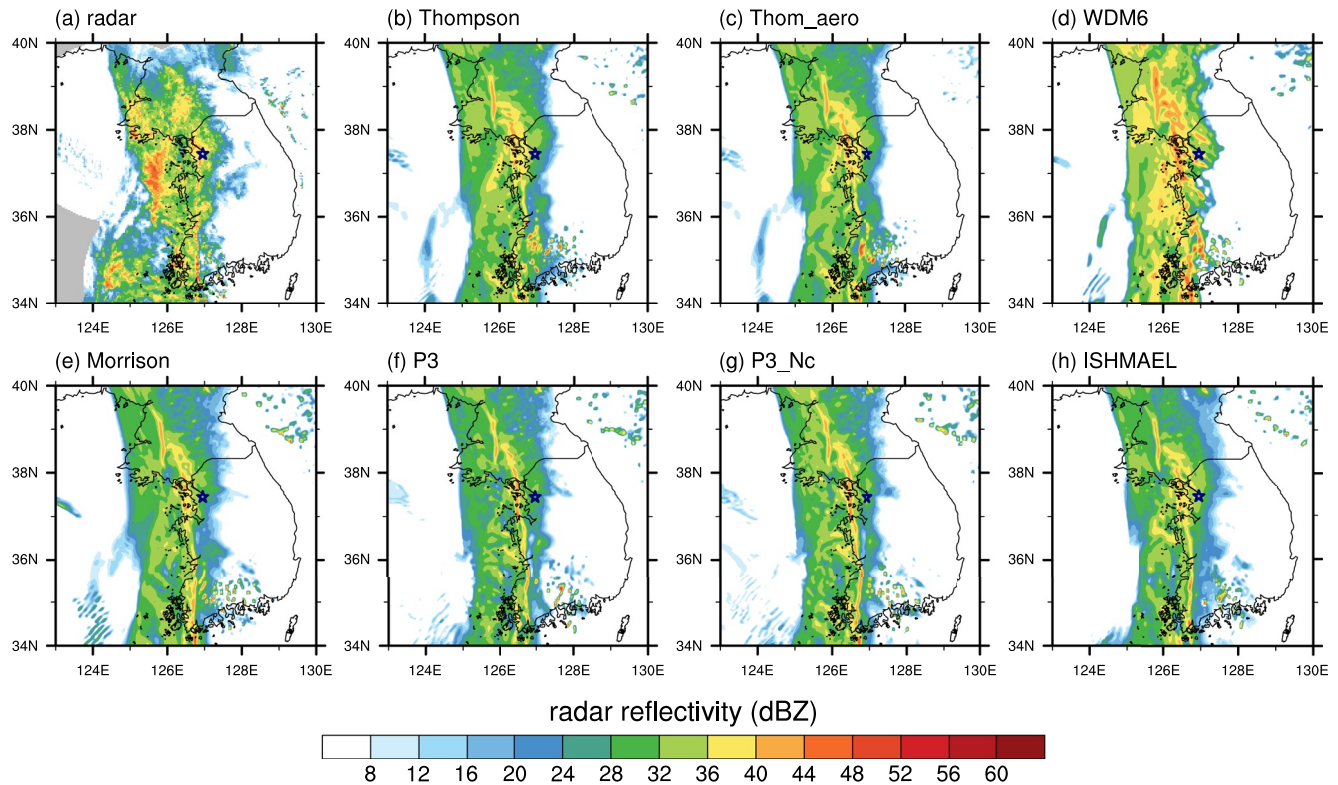


Figure 2. Constant altitude plan position indicator of radar reflectivity at 1.5 km at 0630 LST 8 November 2021, (a) in the multi-radar composite provided by the Korea Meteorological Administration and (b–h) in the simulations using seven different microphysics schemes. The gray areas in (a) are the areas outside of the observation range of radars. The navy star symbol indicates the location of the disdrometer site in Seoul.

low, indicating a developing extratropical cyclone (Figures 1a and 1c). The cold front between the cold dry air mass behind and the warm moist air mass ahead exhibits a large gradient of equivalent potential temperature. As the cold front passes, Seoul experiences an abrupt drop in temperature and a clockwise shift in wind direction (Figures 1c and 1d).

Figure 2a shows the observed horizontal structure of the squall line at 0630 LST, represented by the composite constant altitude plan position indicator (CAPPI) of radar reflectivity at 1.5 km. At this time, a north–south elongated convective line ($\sim 126.8^\circ\text{E}$) reaches Seoul. The convective line is preceded by a relatively weak-echo area and followed by another line of relatively strong echo.

2.2. Model Configuration

To simulate this case, the WRF model version 4.3.3 (Skamarock et al., 2019) is used. Three nested domains are used, which consist of 180×180 , 252×252 , and 252×252 grids horizontally with grid spacing of 27, 9, and 3 km, respectively (Figure 3). Vertically, 49 layers of which the depth is 10 m at the lowest layer and stretches with height are considered for all domains. The domain top height is ~ 20 km (50 hPa). The physics parameterization schemes used in the simulations except for the cloud microphysics scheme are as follows: the Yonsei University (YSU) planetary boundary layer scheme (Hong et al., 2006), the revised MM5 surface layer scheme (Jiménez et al., 2012), the rapid radiative transfer model for general circulation models (RRTMG) scheme (Iacono et al., 2008), the unified Noah land surface model (Tewari et al., 2004), and the Kain–Fritsch cumulus parameterization scheme (Kain, 2004, turned off in the innermost domain). The lateral boundary conditions for the outermost domain and the initial conditions are provided by the European Centre for Medium-Range Weather Forecasts Reanalysis version 5 (ERA5, Hersbach et al., 2020) data, which have a 1-hr temporal resolution and a $0.25^\circ \times 0.25^\circ$ horizontal resolution. The simulations are initialized at 2100 LST 7 November 2021 and integrated until 1200 LST 8, and the outputs are in 1-min intervals. For most of the evaluation and analysis in this study, only the 4-hr period from 0530 to 0930 LST during which Seoul was under direct influence of the squall line is

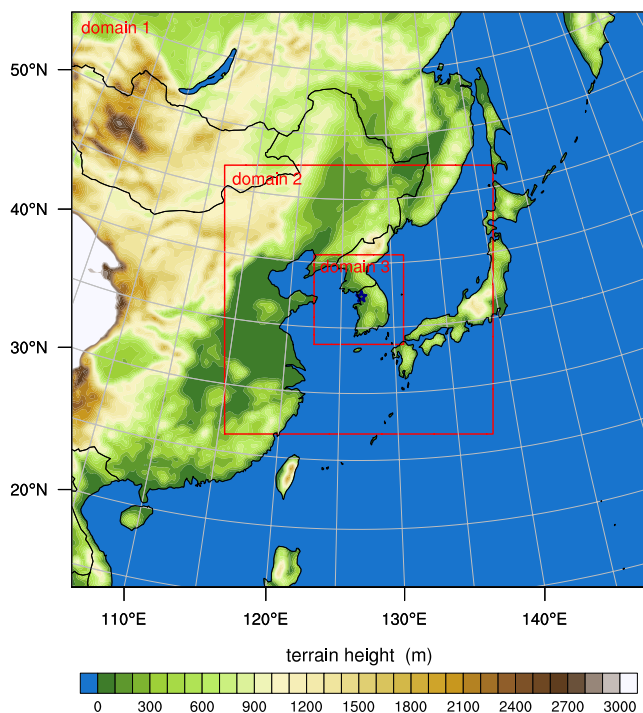


Figure 3. Configuration of three nested domains with terrain height information. The navy star symbol indicates the location of the disdrometer site in Seoul.

considered. Total seven simulations are conducted for this case by employing seven different cloud microphysics options, which are described in the next subsection.

2.3. Microphysics Schemes

The seven different cloud microphysics options used in this study are as follows: the Thompson scheme (G. Thompson et al., 2008), the Thompson aerosol-aware scheme (G. Thompson & Eidhammer, 2014), the WDM6 scheme (Lim & Hong, 2010), the Morrison double-moment scheme (Morrison et al., 2005), two versions of the predicted particle properties (P3) scheme (Morrison & Milbrandt, 2015) with and without the cloud droplet number concentration prediction, and the ice-spheroids habit model with aspect-ratio evolution (ISHMAEL) scheme (Jensen et al., 2017), which correspond to the microphysics option numbers 8, 28, 16, 10, 50, 51, and 55, respectively, in the WRF model configuration. In this study, we regard these seven options as seven different schemes, although the two versions of the P3 scheme share many of their parameterizations with each other. Hereafter, the seven schemes are called the Thompson, Thom_aero, WDM6, Morrison, P3, P3_Nc, and ISHMAEL schemes, respectively.

All of the seven schemes are double-moment schemes for raindrops, prognosing the rainwater mass mixing ratio and the raindrop number concentration, but they differ with each other in terms of assumptions and parameterizations for raindrops and other hydrometeors. Table 1 shows some of the differences among the schemes. For the RSD, all schemes except for the WDM6 scheme assume an exponential distribution, or a gamma distribution with its shape parameter fixed to 0, while the WDM6 scheme assumes a gamma distribution with its shape parameter fixed to 1. For the raindrop terminal velocity–diameter relation, the Thompson and Thom_aero schemes use a gamma distribution function to prevent severe overestimations of terminal velocity of large raindrops, while the others use a power-law function with the exponent of 0.8 (the WDM6, Morrison, P3, and P3_Nc schemes) and 0.5 (the ISHMAEL scheme). Among the seven schemes, the Thom_aero, WDM6, and P3_Nc schemes prognose the cloud droplet number concentration in addition to the cloud water mass mixing ratio, while the other four schemes prognose only the cloud water mixing ratio and assume the cloud droplet number concentration as constant. For the ice hydrometeors, the Thompson, Thom_aero, WDM6, and Morrison schemes follow the conventional approach that classifies them into cloud ice, snow, and graupel categories each

Table 1
Comparisons of the Seven Microphysics Schemes

Schemes	μ	$v(D)$	Prognostic variables		
			Mass mixing ratios	Number concentrations	Others
Thompson	0	$4854D\exp(-195D)$	$q_v, q_c, q_r, q_i, q_s, q_g$	N_r, N_i	
Thom_aero	0	$4854D\exp(-195D)$	$q_v, q_c, q_r, q_i, q_s, q_g$	$N_{CCN}, N_{IN}, N_c, N_r, N_i$	
WDM6	1	$842D^{0.8}$	$q_v, q_c, q_r, q_i, q_s, q_g$	N_{CCN}, N_c, N_r	
Morrison	0	$842D^{0.8}$	$q_v, q_c, q_r, q_i, q_s, q_g$	N_r, N_i, N_s, N_g	
P3	0	$842D^{0.8}$	q_v, q_c, q_r, q_i	N_r, N_i	q_{rim}, B_{rim}
P3_Nc	0	$842D^{0.8}$	q_v, q_c, q_r, q_i	N_c, N_r, N_i	q_{rim}, B_{rim}
ISHMAEL	0	$149D^{0.5}$	$q_v, q_c, q_r, q_{i,k}$	$N_r, N_{i,k}$	$A_{i,k}, C_{i,k}$

Note. μ is the shape parameter in the gamma size distribution of raindrops; $v(D)$ is the raindrop terminal velocity as a function of raindrop diameter D ; q is the mass mixing ratio; N is the number concentration; B is the bulk volume; A and C are the volume-dimensioned mixing ratios. Subscripts “v”, “c”, “r”, “i”, “s”, “g”, “CCN”, “IN”, and “rim” stand for the water vapor, cloud droplets, raindrops, cloud ice, snow, graupel, cloud condensation nucleus aerosols, ice nucleus aerosols, and rime on ice particles, respectively. k in the ISHMAEL scheme is the ice category index ($k = 1, 2, 3$).

of which has a distinct particle density and terminal velocity–diameter relation. Among the four schemes, only the Morrison scheme prognoses the number concentration of precipitating ice particles (i.e., snow and graupel). The P3, P3_Nc, and ISHMAEL schemes, which were relatively recently developed, do not use the predefined categories to classify ice hydrometeors but allow several physical properties of ice hydrometeors to freely evolve in time and space, which prevents artificial conversion between ice hydrometeor categories. For this, the P3 and P3_Nc schemes prognose the rime mass mixing ratio and bulk rime volume and the ISHMAEL scheme prognoses the two volume-dimensioned mixing ratios associated with the two spheroidal axes, in addition to the mass mixing ratio and number concentration of ice particles. Differences in the parameterizations of specific microphysical processes among the seven schemes will be introduced in Section 3.3 when needed. The microphysics schemes are used in their updated version in the WRF model version 4.3.3, which may be slightly different from the original version in the references. It is noted that except for the Thom_aero scheme where a global model simulation data set (Colarco et al., 2010) is used for initial and boundary aerosol data, the default number concentration of cloud condensation nucleus aerosols (WDM6: initially 100 cm^{-3} ; P3_Nc: $3 \times 10^8 \text{ kg}^{-3}$) or cloud droplets (Thompson: 100 cm^{-3} ; Morrison: 250 cm^{-3} ; P3: 200 cm^{-3} ; ISHMAEL: 200 cm^{-3}) for each microphysics scheme is used.

2.4. Disdrometer Data

The simulation outputs are evaluated using data from a Parsivel² disdrometer (Tokay et al., 2014) installed at Seoul National University (37.45°N , 126.95°E ; marked in Figures 1–3). This optical disdrometer measures the diameter and fall velocity of hydrometeor particles that pass through its sampling volume (a $180\text{-mm} \times 30\text{-mm}$ laser sheet with 1-mm height) between the transmitter and receiver of 650-nm -wavelength laser beams, based on the maximum attenuation and duration of the laser beam signals. The measurements are recorded as particle numbers in 32×32 bins, which correspond to 32 non-equidistant diameter classes ($0\text{--}26 \text{ mm}$) and 32 non-equidistant fall velocity classes ($0\text{--}22.4 \text{ m s}^{-1}$). In this study, data that are classified as liquid precipitation and correspond to the diameter classes between the third and 23rd classes ($0.25\text{--}8 \text{ mm}$) are used. The temporal resolution of the data is 1 min , same as the output interval of simulations. To eliminate spurious data caused by various reasons such as strong winds and drop splashing, quality control is conducted using methods suggested by previous studies (e.g., Jaffrain & Berne, 2011; Jwa et al., 2021): the drops with fall velocities 60% larger or smaller than the reference velocities (the terminal velocity–diameter relation of Atlas et al. (1973)) are excluded from the data. Also, only the data with rain rate and total drop counts greater than or equal to 0.05 mm hr^{-1} and 100, respectively, are used for the analysis if they persist for three or more minutes consecutively, following E. J. Thompson et al. (2015). In J. Lee et al. (2022), the data from this disdrometer at Seoul National University were validated by comparing the measured hourly rain amounts with those observed by the collocated rain gauge for $\sim 3\text{-year}$ period from 2018 to 2021, and the correlation coefficient was 0.99, demonstrating the high reliability of these data.

2.5. RSD Parameters

For evaluation, RSD parameters are computed from both the disdrometer data and simulation outputs. From the disdrometer data, the RSD is obtained for each 1-min data as follows:

$$N(D_i) = \sum_{j=1}^{32} \frac{n_{ij}}{A_i V_j \Delta t \Delta D_i}, \quad (1)$$

where $N(D_i)$ is the raindrop number concentration per unit volume per unit size interval for the i th diameter class ($\text{m}^{-3} \text{ mm}^{-1}$), n_{ij} is the raindrop number recorded in the i th diameter and j th fall velocity classes, A_i (m^2) is the effective disdrometer sampling area for the i th diameter class, V_j (m s^{-1}) is the fall velocity of the j th fall velocity class, Δt (s) is the sampling interval, and ΔD_i is the diameter interval of the i th diameter class. D_i is the mid-value of the i th diameter class. The rain rate R (mm h^{-1}) is computed as

$$R = 6\pi \times 10^{-4} \sum_{i=3}^{23} \sum_{j=1}^{32} D_i^3 \frac{n_{ij}}{A_i \Delta t}. \quad (2)$$

The n th-order moment of RSD M_n ($\text{m}^{-3} \text{ mm}^n$) is calculated as

$$M_n = \sum_{i=3}^{23} D_i^n N(D_i) \Delta D_i. \quad (3)$$

Using the RSD moments, the mass-weighted mean diameter D_m (mm) and the generalized intercept parameter N_w ($\text{m}^{-3} \text{mm}^{-1}$) are calculated as follows:

$$D_m = \frac{M_4}{M_3}, \quad (4)$$

$$N_w = \frac{4^4}{\Gamma(4)} \left(\frac{M_3}{D_m^4} \right), \quad (5)$$

where $\Gamma(s)$ is the gamma function. Note that N_w of an RSD is defined as the intercept parameter of an exponential RSD that has the same values of rainwater mass content and D_m as the original RSD (Testud et al., 2001).

From the simulation outputs in 1-min intervals, the gamma RSD is constructed from two prognostic variables, the rainwater mixing ratio q_r (g kg^{-1}) and the (total) raindrop number concentration N_r (kg^{-1}), as it is done in each microphysics scheme:

$$N(D) = N_0 D^\mu \exp(-\Lambda D), \quad (6)$$

where N_0 ($\text{m}^{-3} \text{mm}^{-1-\mu}$), μ , and Λ (mm^{-1}) are the intercept parameter, shape parameter, and slope parameter, respectively. In the seven microphysics schemes, μ is constant (Table 1), and N_0 and Λ are computed using q_r and N_r :

$$N_0 = \frac{\Lambda^{\mu+1} \rho_a N_r}{\Gamma(\mu+1)}, \quad (7)$$

$$\Lambda = \left[\frac{\Gamma(\mu+4)}{\Gamma(\mu+1)} \frac{\pi \rho_w}{6} \frac{N_r}{q_r} \right]^{\frac{1}{3}}. \quad (8)$$

Here, ρ_a (kg m^{-3}) is the density of air and ρ_w (g mm^{-3}) is the density of liquid water. Once the RSD is obtained, the RSD moments can be calculated by integration:

$$M_n = \int D^n N(D) dD. \quad (9)$$

In the original definition of M_n , the lower limit of the integral is zero. However, to enable a fair quantitative evaluation using the RSD moments calculated from the disdrometer data where raindrops with diameter smaller than 0.25 mm are not included, the lower limit of the integral is set to be 0.25 mm in the M_n calculation from the simulation outputs:

$$M_n = \int_{D^*}^{\infty} D^n N(D) dD = \frac{N_0 \Gamma(\mu+n+1, \Lambda D^*)}{\Lambda^{\mu+n+1}}, \quad (10)$$

where D^* is 0.25 mm and $\Gamma(s, x)$ is the upper incomplete gamma function. Note that M_0 and M_3 are directly related to N_r and q_r , respectively. Based on M_3 and M_4 calculated using Equation 10, D_m and N_w in the simulations are obtained using Equations 4 and 5, respectively. Note that all RSD moments and parameters are calculated at the lowest grid box that includes the location of the disdrometer site.

3. Results and Discussion

3.1. General Results

In all seven simulations, the passing of the cold front that drives the squall line is successfully reproduced, but with a slight delay. The simulated time series of sea-level pressure, near-surface temperature, and wind direction are compared to the observation at an automatic weather station (located ~5 km northwest of the disdrometer site) operated by the Korea Meteorological Administration (Figure 4). As the cold front approaches, the observed sea-level pressure steadily decreases and reaches the minimum at 0640 LST, and rises after the cold front arrives. The pattern is well reproduced in the simulations, while the time of sea-level pressure minimum is delayed

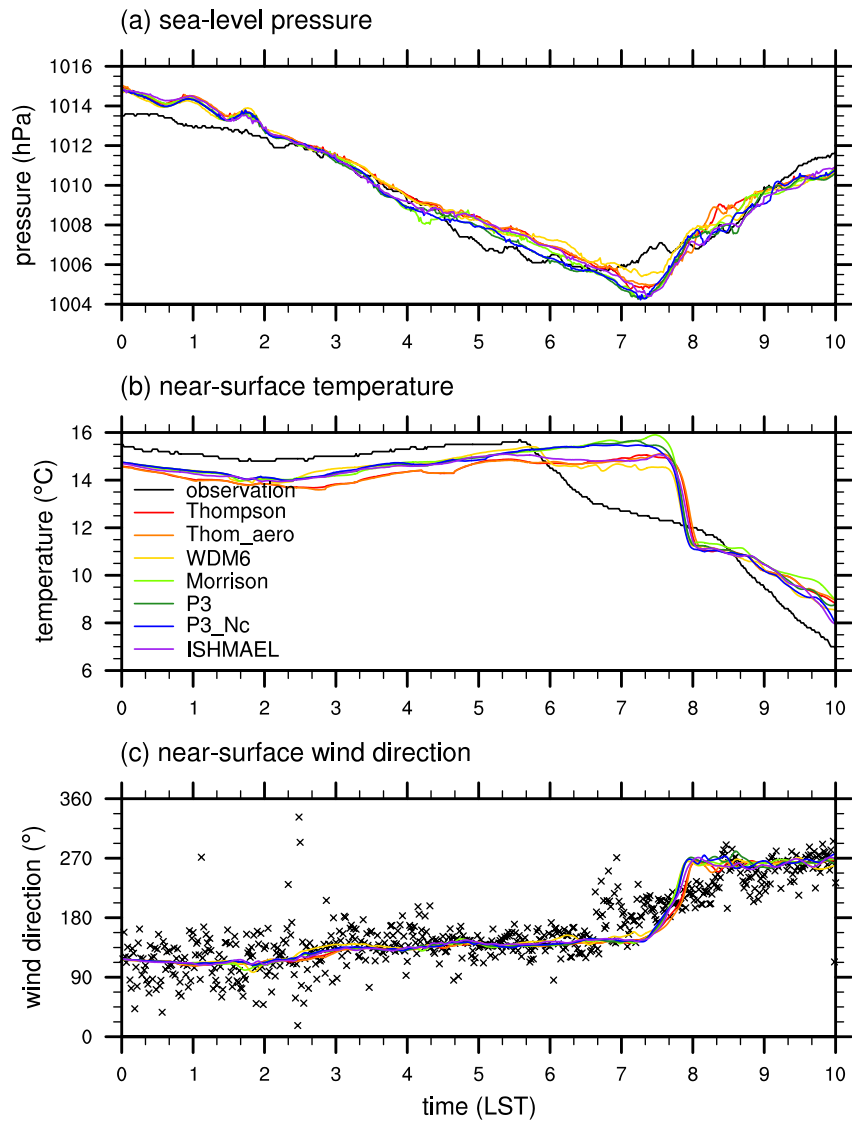


Figure 4. Time series of (a) sea-level pressure, (b) near-surface temperature, and (c) near-surface wind direction in the observation and simulations at the automatic weather station (37.49°N, 126.92°E) ~5 km northwest of the disdrometer site. For the simulations, the values at a grid box that includes the location of the automatic weather station are shown. In (c), the observed values are indicated by cross marks.

by 40 min, which indicates that the arrival of the cold front is delayed. The observed near-surface temperature starts to drop from 0540 LST in accordance with the beginning of precipitation, showing a steep slope (-2.8 K hr^{-1}) until 0630 LST. Then the slope becomes gentle (-0.9 K hr^{-1}) until 0820 LST, and becomes steep again (-2.8 K hr^{-1}) after that due to the cold advection. In the simulations, the near-surface temperature does not decrease until 0740 LST and then suddenly drops within a short time until 0800 LST (-10.5 K hr^{-1} , averaged over the seven simulations). The 2-hr delay of temperature drop is even longer than the 40-min delay of pressure minimum, which may indicate that evaporative cooling from precipitation is underestimated in the simulations. After the sudden drop, the near-surface temperature decreases slowly (-0.8 K hr^{-1}) until 0840 LST and exhibits a faster decrease (-1.4 K hr^{-1}) afterward. The observed near-surface wind direction changes from southeasterly to westerly as the cold front passes, and this change is well reproduced in the simulations although the simulated change occurs more drastically within a relatively short time.

Figures 2b–2h show the horizontal structures of the simulated squall lines at 1.5 km at 0630 LST. In all simulations, the north–south elongated shape of the squall line is successfully reproduced. At this time, the convective

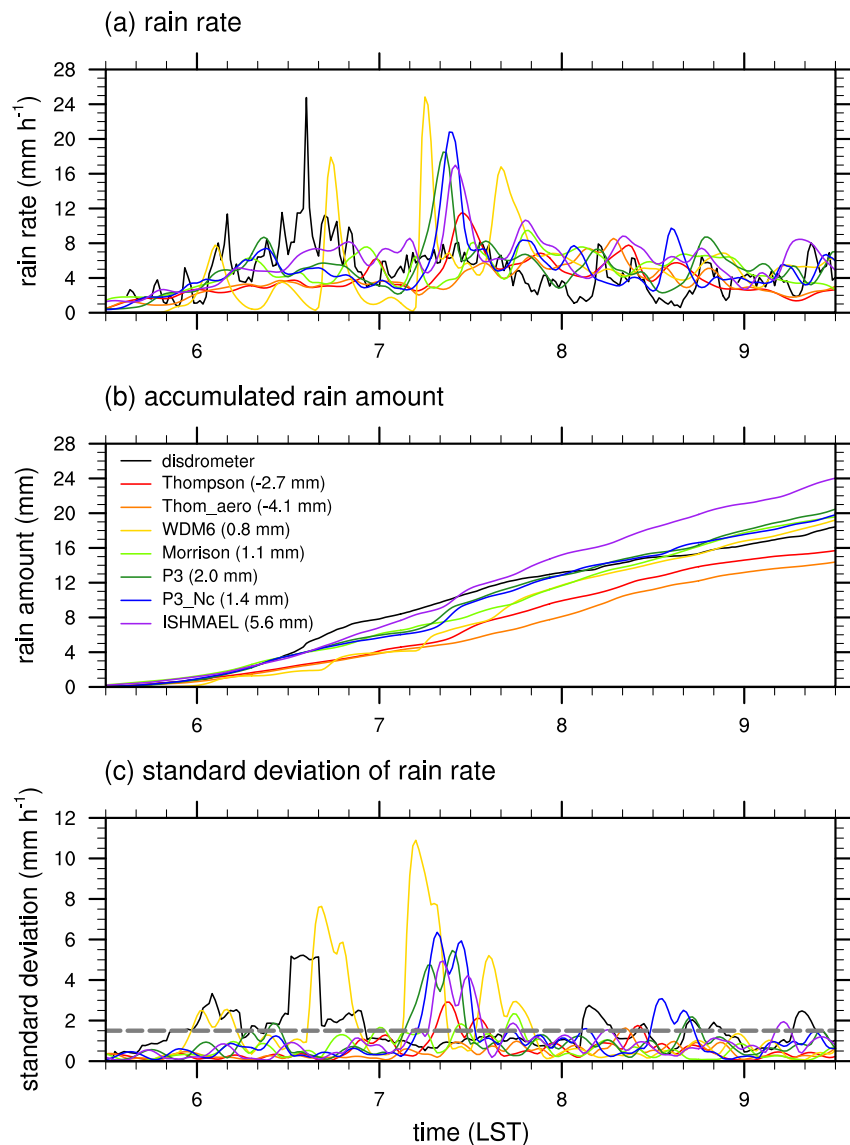


Figure 5. Time series of (a) rain rate, (b) accumulated rain amount, and (c) 10-min standard deviation of rain rate at the disdrometer site in the observation and simulations. The values in parentheses in (b) are the biases of 4-hr accumulated rain amount. The gray dashed line in (c) indicates the standard deviation of 1.5, which is used to identify convective precipitation.

line has arrived Seoul in the observation, while those in the simulations have not arrived yet, which is associated with the delayed passing of the cold front. The horizontal structures of the simulated squall lines are overall similar to each other, except for the WDM6 simulation. The WDM6 simulation not only shows overall higher radar reflectivity than the other simulations but also exhibits multiple convective cells ahead and behind of the convective line, which do not appear in the other simulations. The P3 and P3_Nc simulations show narrower and more distinct convective line than the other simulations, which is consistent with the results of squall line simulations in Morrison et al. (2015), due to its capability of simulating high-density ice particles and resultant heavy precipitation.

Figure 5 shows the time series of observed and simulated rain rate, accumulated rain amount, and 10-min standard deviation of rain rate at the disdrometer site during the analysis period of 0530–0930 LST. Rain rate is very small at the beginning of the analysis period and increases with time with some fluctuations both in the observation and in the simulations (Figure 5a). The maximum rain rate appears at 0636 LST in the observation, while it appears at 0710–0730 LST in the simulations (except for the Thom_aero and Morrison simulations),

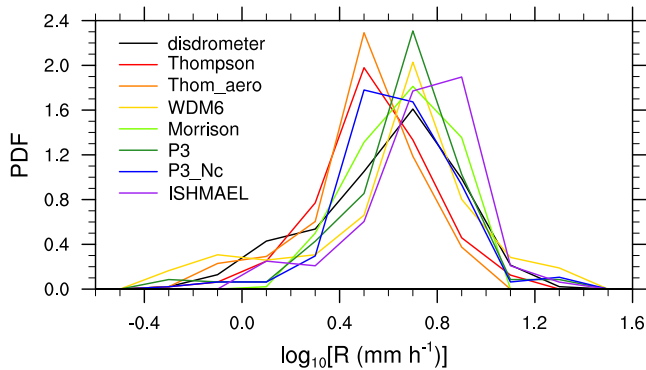


Figure 6. Probability density functions of the logarithm of rain rate at the disdrometer site during the analysis period of 0530–0930 LST in the observation and simulations.

which is attributed to the delayed arrival of the convective line. The sudden increase in rain rate when the convective line passes does not occur in the Thom_aero and Morrison simulations. The WDM6 simulation shows much stronger fluctuation of rain rate than the other simulations until ~0800 LST, which is associated with the convective cells ahead and behind of the convective line (Figure 2d).

The temporal variability of rain rate has implications on the rain type. Bringi et al. (2003) classified convective and stratiform rain types using the 10-min standard deviation of rain rate. If the standard deviation exceeds 1.5 mm hr^{-1} , rain is classified as convective, and otherwise, it is classified as stratiform. According to this classification, rain that is observed or simulated when the convective line passes the disdrometer site (~0620–0700 LST in the observation and ~0710–0740 LST in the simulations) is actually classified as convective, except for the Thom_aero and Morrison simulations (Figure 5c). Stratiform rain is predominant before and after the passing of convective line, in both the observation and most of the simulations. In the WDM6 simula-

tion, convective rain occurs multiple times before and after the passing of convective line. The 4-hr accumulated rain amount observed by the disdrometer is 18 mm, and all seven simulations reasonably well reproduce it, ranging from 14 to 24 mm (Figure 5b).

Although the simulations have disagreements with the disdrometer observation on the time of large rain rates associated with convective rain, the distributions of simulated rain rates in the analysis period are comparable to the disdrometer observation. Figure 6 shows the probability density functions (PDFs) of the logarithms of rain rates $\log_{10}R$ at the disdrometer site in the observation and simulations. The modal value of $\log_{10}R$ in the observation is 0.7, and it coincides with those in the WDM6, Morrison, and P3 simulations (0.7) and is close to those in the other simulations (0.5 for the Thompson, Thom_aero, and P3_Nc simulations and 0.9 for the ISHMAEL simulation). This indicates that except for some temporal mismatches, the simulations successfully reproduce the variation of mass flux of rain at the surface.

3.2. Evaluation of Simulated Raindrop Number Concentration and Other RSD Parameters

The successful predictions of rain mass flux at the surface in the simulations shown in the previous subsection encourage a further level of evaluation, that is, whether the simulations reasonably predict how the rain mass is distributed in size (i.e., RSD). The evaluation of simulated RSD characteristics will give implications on whether the double-moment rain microphysics is operating reasonably. Considering that the rain rate is well predicted in all simulations, if a simulation shows RSD characteristics that are significantly biased from the observation, it is implied that the simulation has not benefited from the double-moment treatment of raindrops despite the expense of additional computational resources and that the microphysics scheme used in the simulation may contain severe deficiencies in the parameterizations of raindrop number-related microphysical processes.

The performances of the double-moment microphysics schemes in predicting the raindrop number concentration and other RSD parameters are evaluated using the ground-based disdrometer data. As in Figure 6, the evaluations are conducted by comparing PDFs of RSD parameters obtained using the entire data during the analysis period rather than directly comparing their time series, which prevents the slight temporal mismatches between the observation and simulations from undermining the validity of the evaluations. Figure 7 shows the PDFs of the logarithms of RSD moments from M_0 to M_6 at the disdrometer site in the observation and simulations. Note that among these RSD moments, only M_0 and M_3 are prognostic moments while the others are diagnosed using the prognostic moments. Although the evaluation of the prognostic moments is of the most importance, the diagnostic moments also deserve evaluation because each of them is closely associated with specific microphysical process rates parameterized in the microphysics schemes. A poor diagnosis on these moments leads to a poor estimation of relevant microphysical process rates.

For M_3 (Figure 7d), the primary prognostic RSD moment in bulk microphysics schemes, the seven microphysics schemes show the best agreement with each other and with the observation, compared to the other RSD moments. The modal value of the observed $\log_{10}M_3$ is 2.8, which coincides with the modal values of $\log_{10}M_3$ in the WDM6

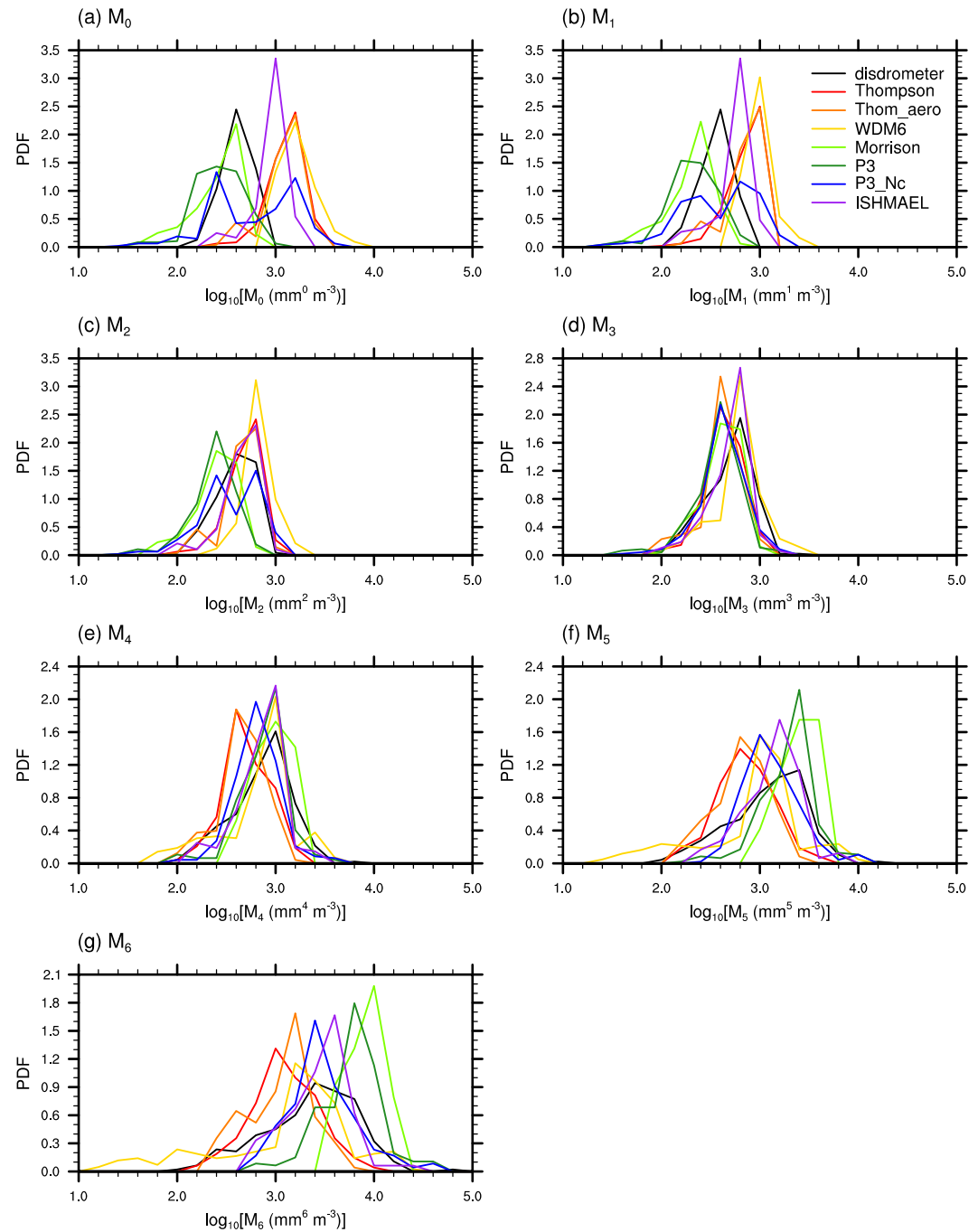


Figure 7. Probability density functions of the logarithms of RSD moments from M_0 to M_6 at the disdrometer site during the analysis period of 0530–0930 LST in the observation and simulations.

and ISHMAEL simulations. The predicted distribution of M_3 in the rest of the simulations are also similar to the observation: the modal value of $\log_{10}M_3$ is 2.6 in these simulations. The rainfall case selected in this study is a case for which all of the microphysics schemes show ideal performances for the prediction of M_3 , similar to the performances for the prediction of rain rate shown in the previous subsection.

For M_0 (Figure 7a), another prognostic RSD moment, the PDFs from the simulations are distinguished from each other, and many of them are significantly deviated from the observation. The observed $\log_{10}M_0$ is mostly distributed between 2.3 and 2.9, with its modal value being 2.6. The Thompson, Thom_aero, and WDM6 schemes

greatly overestimate M_0 , with the modal values of $\log_{10}M_0$ being 3.2, indicating four times larger M_0 compared to the observation. Most of the $\log_{10}M_0$ in those three simulations is larger than 2.9, indicating clear differentiation from the observation. Although not much as the three schemes, the ISHMAEL scheme also overestimates M_0 , with the modal value of $\log_{10}M_0$ being 3.0. The Morrison scheme gives the $\log_{10}M_0$ PDF that is closest to the observation, showing the modal value coincident with that for the observation, but the distribution is overall negatively biased, mostly placed between 2.1 and 2.7. The P3 scheme, which shares most of the warm-rain microphysical parameterizations with the Morrison scheme, also gives a negatively biased distribution of $\log_{10}M_0$ showing the modal value of 2.4. The P3_Nc scheme shows two prominent peaks in the $\log_{10}M_0$ distribution at 2.4 and 3.2: one is smaller and the other is much larger than the modal value of observed $\log_{10}M_0$. Note that the P3_Nc scheme partially agrees with the P3 scheme in the sense that one of the two modes for the P3_Nc scheme has the modal value of $\log_{10}M_0$ identical to that for the P3 scheme, but the other mode is a totally new feature that is not seen for the P3 scheme. The dramatic difference in the M_0 prediction between the P3 and P3_Nc schemes indicates that the double-moment treatment for cloud droplets can have a significant impact on the raindrop number prediction. An opposite example also exists, that is, the Thompson and Thom_aero schemes, which show very similar predictions for M_0 despite their different treatments for cloud droplets.

As the order of moment increases from 0 to 3, the PDFs of the simulated RSD moments converge gradually and become closer to that of the observed RSD moment. As for M_0 , for M_1 and M_2 (Figures 7b and 7c), the Thompson, Thom_aero, WDM6, and ISHMAEL schemes show positively biased PDFs of the logarithms, while the Morrison and P3 schemes show negatively biased PDFs. The rainwater evaporation rate is often parameterized using $M_{1+\mu}$ and $M_{1.5+b+\mu}$ (e.g., Cohard & Pinty, 2000; Rutledge & Hobbs, 1983), where b is the exponent in the power-law type raindrop terminal velocity relation $v(D) = aD^b$. This implies that the microphysics schemes that overestimate (underestimate) M_1 and M_2 and assume the shape parameter of RSD as 0 may also overestimate (underestimate) the rainwater evaporation rate. RSD moments close to M_3 ($M_{2+b+\mu}$) or M_3 itself are generally used in the parameterization of accretion of cloud droplets by raindrops (e.g., Hong & Lim, 2006; Seifert & Beheng, 2001). The increasing similarity between the simulated and observed RSD moments around M_3 contributes to more accurate representation of the accretion process in the simulations.

As the order of moment further increases from 3, the PDFs of the simulated RSD moments gradually diverge from each other and mostly from the observed RSD moment (Figures 7e–7g). For M_6 (Figure 7g), the difference between the smallest and largest modal values of $\log_{10}M_6$ among the schemes is 1, which shows the difficulties in the prediction of high-order RSD moments using double-moment microphysics schemes. It is noteworthy that the schemes that greatly overestimate M_0 (the Thompson, Thom_aero, and WDM6 schemes) show negatively biased PDFs of $\log_{10}M_6$ and the schemes that give negatively biased PDFs of $\log_{10}M_0$ (the Morrison and P3 schemes) show positively biased PDFs of $\log_{10}M_6$. This is not surprising because the simulated M_6 is a diagnostic RSD moment that is proportional to $M_3^2 M_0^{-1}$. These results show that for double-moment microphysics schemes to make reasonable predictions of high-order RSD moments, accurate predictions of M_0 as well as M_3 is essential. The P3_Nc and ISHMAEL schemes give the $\log_{10}M_6$ PDFs that are closest to the observation.

In addition to accurate predictions of M_0 and M_3 , the appropriateness of the RSD assumptions in the microphysics scheme is another crucial factor for the accurate predictions of high-order RSD moments. In the double-moment microphysics schemes, the diagnosis of M_6 from M_0 and M_3 is made as follows:

$$M_6 = k M_3^2 M_0^{-1}, \quad (11)$$

$$k = \frac{(\mu + 6)(\mu + 5)(\mu + 4)}{(\mu + 3)(\mu + 2)(\mu + 1)}. \quad (12)$$

For gamma RSDs, k depends solely on μ (monotonically decreasing with increasing μ , when $\mu \geq 0$), which makes it a constant in the seven schemes where μ is a constant. However, in the relationship between the RSD moments in reality, k can be highly variable because of the variation of μ and the limitation of gamma RSD assumption itself. Figure 8 shows the PDF of $\log_{10}k$ calculated from Equation 11 in the observation and simulations. Note that $\log_{10}k$ in the simulations is not completely invariable due to the lower limit applied to the integral in the calculation of the RSD moments (see Equation 10). The observed $\log_{10}k$ is overall much smaller than the simulated $\log_{10}k$, implying that the constant μ used in the seven schemes (0 or 1) may be too small. The choice of $\mu = 1$ in the WDM6 scheme yields not satisfactory prediction of $\log_{10}k$, but it is absolutely better than the predictions by

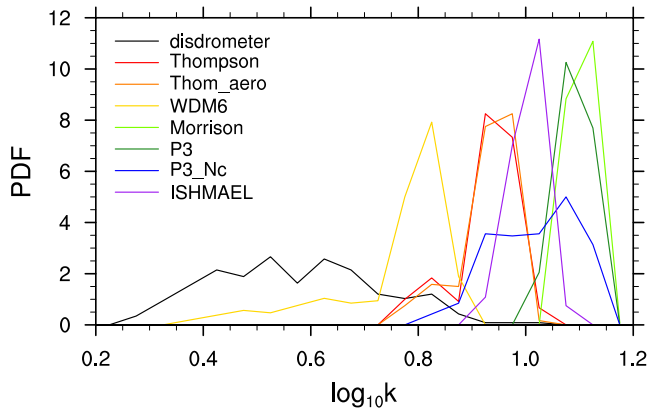


Figure 8. Probability density functions of $\log_{10}k$ calculated from Equation 11 at the disdrometer site during the analysis period of 0530–0930 LST in the observation and simulations.

other schemes assuming $\mu = 0$, which is the reason why the WDM6 scheme shows a less biased $\log_{10}M_0$ PDF than the Thompson scheme despite its relatively poor performance in the M_0 prediction. The large variability of the observed $\log_{10}k$ suggests that to better predict high-order RSD moments in double-moment microphysics schemes, the use of diagnostic relations for μ that allow its variation (e.g., Cao et al., 2008) may be helpful. Choosing a different pair of prognostic RSD moments other than M_0 and M_3 can also improve the predictions of high-order RSD moments (Morrison et al., 2019).

Figure 9 shows the PDFs of two parameters that are widely used to characterize RSD, the mass-weighted mean diameter D_m and the logarithm of generalized intercept parameter $\log_{10}N_w$. The observed D_m and $\log_{10}N_w$ are mostly distributed within 0.8–2.2 mm and 3.1–4.1, respectively. For the two RSD parameters, the microphysics schemes show severe disagreement with each other and most of their PDFs are largely deviated from the observation. The predictions of D_m and $\log_{10}N_w$ by each scheme are closely associated with the prediction of M_0 . The Thompson, Thom_aero, and WDM6 schemes that give positively biased distributions for M_0 significantly underestimate D_m and overestimate $\log_{10}N_w$. For the three schemes, D_m larger than 1.5 mm,

which accounts for 53% of the observed D_m , is rarely seen. In contrast, the Morrison and P3 schemes that give negatively biased distributions for M_0 largely overestimate D_m and underestimate $\log_{10}N_w$. The modal values of the simulated D_m for the two schemes are both 2.1 mm, which is 0.6 mm larger than that of the observed D_m . The P3_Nc scheme gives much wider distributions of D_m and $\log_{10}N_w$ than the observation. The ISHMAEL scheme gives most realistic D_m and $\log_{10}N_w$ distributions among the seven schemes, which is partly attributable to the scheme's relatively realistic representation of M_3 – M_0 relationship (see Figure 11). It is also attributable to that for this scheme, the D_m and $\log_{10}N_w$ biases originating from M_0 predictions happen to be counterbalanced by those originating from the inappropriateness in the RSD assumption, which is not the case of the Morrison and P3 schemes (not shown).

Given the importance of M_0 prediction, the characteristics of M_0 prediction of each scheme deserve further investigation. Average M_0 is computed for each of different rain rate bins and M_3 bins to show how M_0 is related to rain rate and M_3 (Figure 10). In the observation, average M_0 almost does not change for the first two rain rate bins and gradually increases afterward (Figure 10a). However, most of the schemes show relatively steep increases in average M_0 for small rain rate bins. The WDM6 scheme shows a nearly constant average M_0 for the first two rain rate bins, similar to the observation, but shows a decrease in average M_0 from the second to fifth rain rate bin, which is opposite to the observation. The P3_Nc scheme shows too dramatic changes in average M_0 , including a steep increase followed by a decrease, both of which are not seen in the observation. For the relationship between M_0 and M_3 , the microphysics schemes except for the WDM6 scheme show increases in average M_0 with M_3 as in the observation, but the increases from the second to third M_3 bin is relatively steep compared to the observation (Figure 10b). The WDM6 scheme shows a decrease in average M_0 with M_3 from the second to fourth M_3 bin, again opposite to the observation.

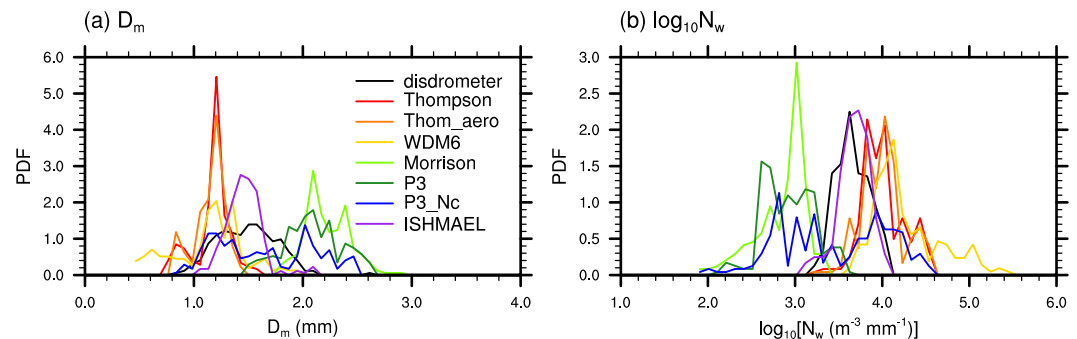


Figure 9. Probability density functions of (a) D_m and (b) $\log_{10}N_w$ at the disdrometer site during the analysis period of 0530–0930 LST in the observation and simulations.

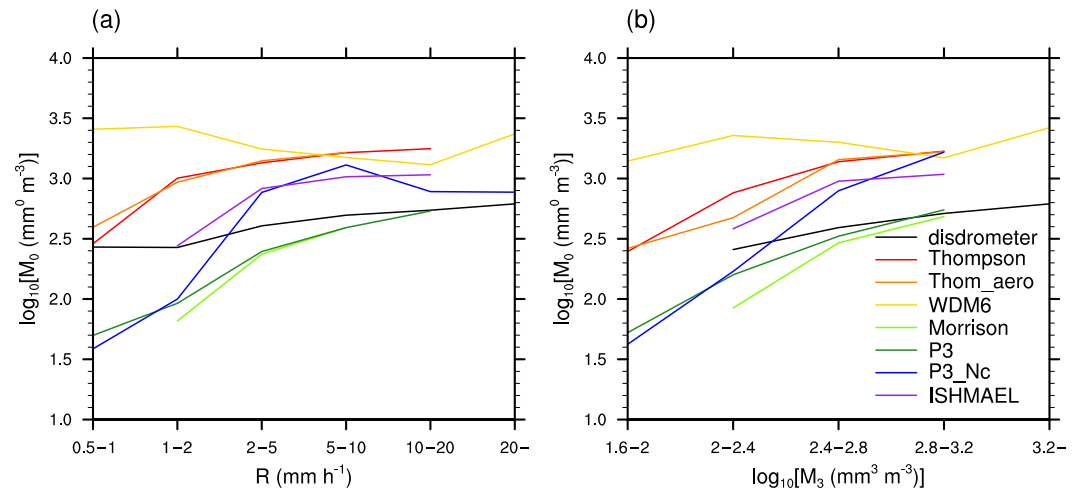


Figure 10. Logarithm of average M_0 computed for (a) different rain rate bins and (b) different $\log_{10}M_3$ bins at the disdrometer site during the analysis period of 0530–0930 LST in the observation and simulations.

To evaluate the relationship between M_0 and M_3 in the simulations in more detail, scatter plots including time information are presented in the $\log_{10}M_3$ – $\log_{10}M_0$ space (Figure 11). The earlier period of rainfall that corresponds to the front part of the precipitation system is colored in red and orange, and the later period of rainfall that corresponds to the rear part of the system is colored in green and blue. Throughout the analysis period, the observed $\log_{10}M_3$ – $\log_{10}M_0$ pairs are distributed in the vicinity of a straight line toward the upper right (M_3 increasing with M_0). This indicates that in the observation, the M_3 – M_0 relationship remains almost the same for this precipitation system, regardless of changes in M_3 with time associated with different parts of the system. The Thompson and Thom_aero schemes show linear-like relationships between $\log_{10}M_3$ and $\log_{10}M_0$ in the front part of the system but show a jump of $\log_{10}M_0$ in the rear part of the system, which gives larger $\log_{10}M_0$ for given $\log_{10}M_3$ than in the front part. The WDM6 scheme shows an undefinable distribution of $\log_{10}M_3$ – $\log_{10}M_0$ pairs, which is totally different from the observation. The reason for the distinctive M_3 – M_0 (Figures 10b and 11d) and R – M_0 (Figure 10a) relationships of the WDM6 scheme is that this scheme fails to reproduce active raindrop production via collision–coalescence (autoconversion) that occurs in the convective parts of the squall line where M_3 and R are large (Ferrier et al., 1995; Morrison et al., 2009), which should have built positive correlations of M_0 with M_3 and R . This will be shown in Section 3.3. The Morrison, P3, P3_Nc, and ISHMAEL schemes all show front-part $\log_{10}M_3$ – $\log_{10}M_0$ relationships close to linear and rear-part relationships distinguishable from the former. Especially, the P3_Nc scheme shows a big jump of M_0 from the front part to the rear part of the system, which is very far from the observation. The discrepancy in the M_3 – M_0 relationship that is relatively constant in the observation and relatively varying in the simulations indicates that the variability of this relationship during this rainfall case is exaggerated in the simulations.

For the first half of the analysis period, which is before the jump of $\log_{10}M_0$ occurs for the most schemes, the linear regression of $\log_{10}M_0$ on $\log_{10}M_3$ is obtained. The slope value in the observation is 0.55, and that in the ISHMAEL scheme (0.65) is closest to the observation, followed by those in the Thompson (0.76), P3 (0.76), Thom_aero (0.84), and P3_Nc (0.93) schemes. The relatively accurate representation of M_3 – M_0 relationship by the ISHMAEL scheme is one of the reasons why this scheme shows the most realistic predictions of M_6 , D_m , and $\log_{10}N_w$. On the contrary, the Morrison scheme shows the steepest slope among the seven schemes (1.15), which may be attributed to the relatively large contribution of autoconversion to the N_r budget (will be shown in Section 3.3). This is one of the reasons why this scheme shows biased predictions of D_m and $\log_{10}N_w$ for which the M_3 – M_0 relationship is important.

The evaluation of simulated raindrop number concentration and other RSD parameters in this subsection has been done by comparing the simulation data (accumulated over the 4-hr analysis period) from the grid box that includes the location of the disdrometer site against the observation data at the disdrometer site. Although it is shown in Figure 2 that the spatial distribution of the squall line is reasonably well simulated by all schemes, there may exist spatial biases of several tens of kilometers in the simulated squall lines that are not detected from

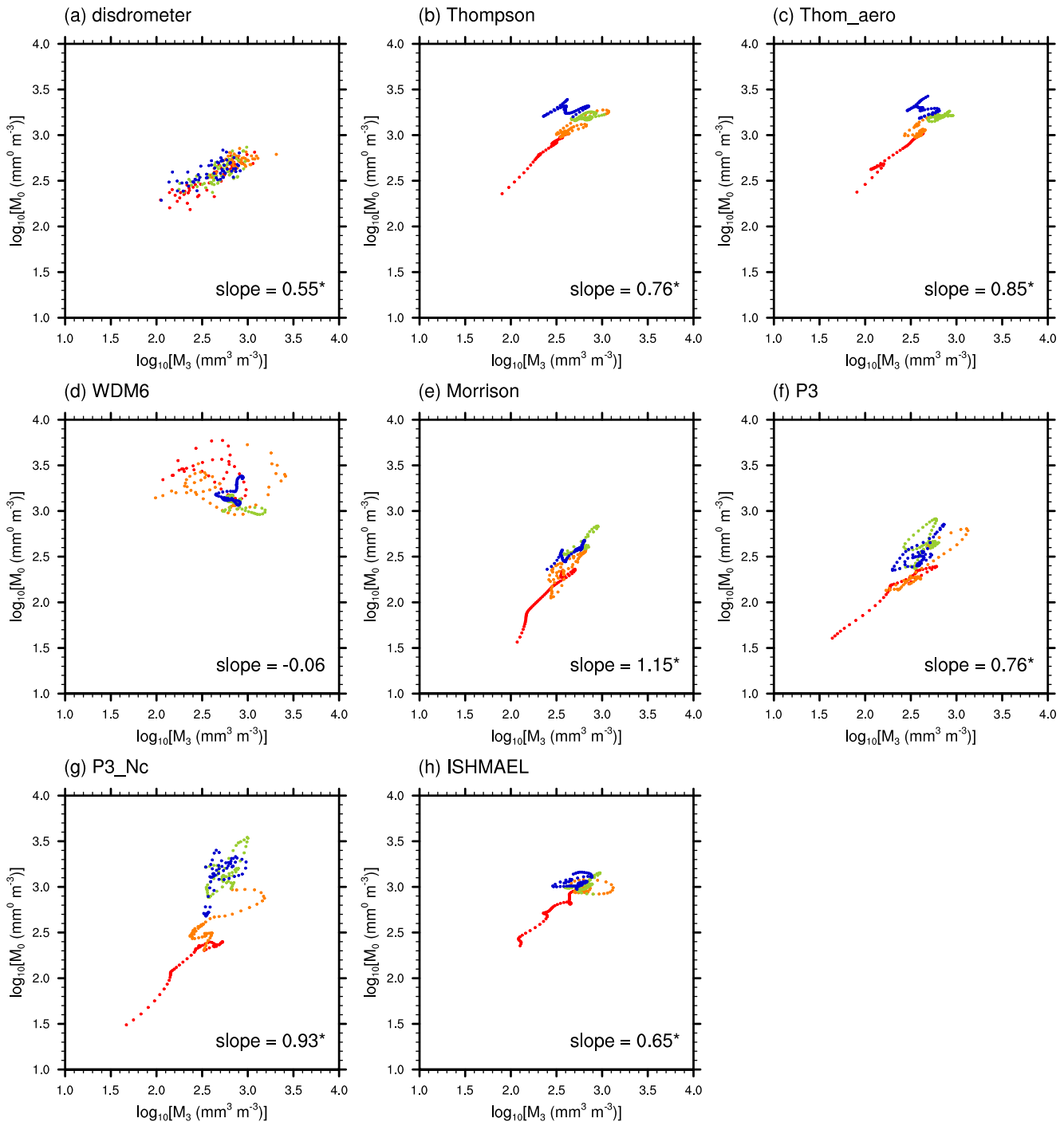


Figure 11. Scatter plots of $\log_{10}M_3$ and $\log_{10}M_0$ at the disdrometer site in the (a) observation and (b–h) simulations. The red, orange, green, and blue colors indicate the time periods of 0530–0630 LST, 0630–0730 LST, 0730–0830 LST, and 0830–0930 LST, respectively. The slope value of the linear regression of $\log_{10}M_0$ on $\log_{10}M_3$ for the first half of the analysis period (0530–0730 LST) is indicated in each subfigure. The asterisk indicates statistical significance at the confidence level of 95%.

Figure 2. If the simulated RSD characteristics during the analysis period have significant spatial variability within the squall line, the spatial uncertainty of the simulations could undermine the validity of the evaluation. Figure 12 shows the $\log_{10}M_0$ PDFs in the observation and simulations, which is identical to Figure 7a except that those in the simulations are obtained using data from areas of different sizes centered at the disdrometer site. As can be expected from the squall line's shape that is quite homogeneous in the meridional direction, the $\log_{10}M_0$ PDFs obtained from meridionally 27- and 201-km long arrays of grid boxes for each simulation and their biases from

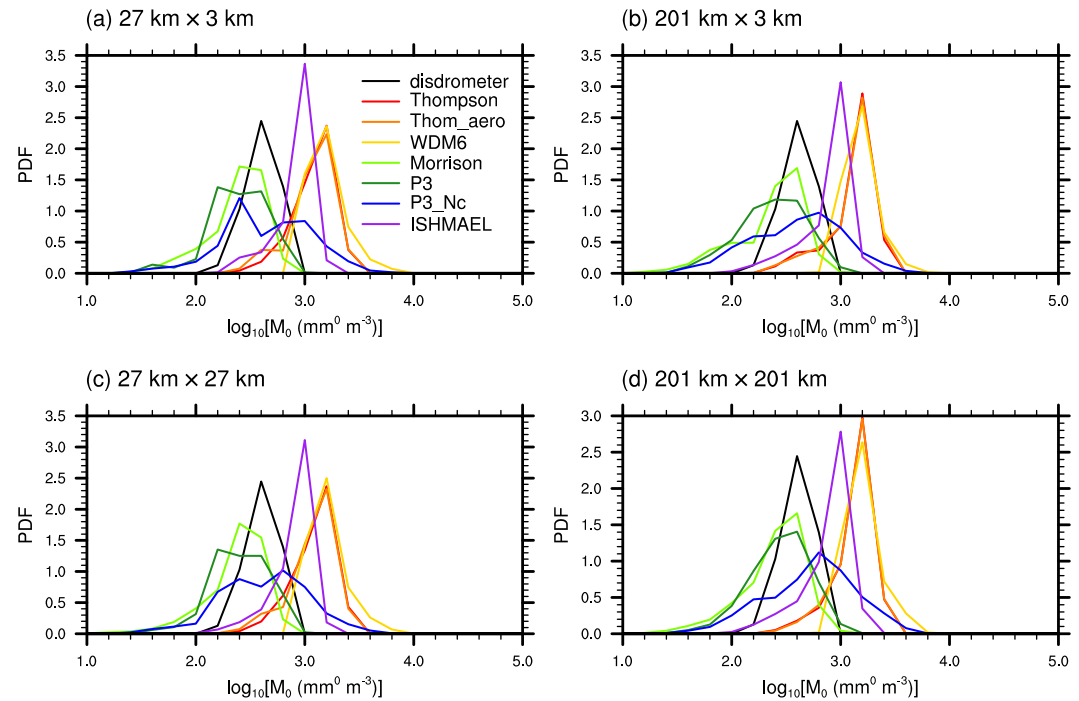


Figure 12. Probability density functions of $\log_{10}M_0$ during the analysis period of 0530–0930 LST in the observation and simulations. The observation data are from the disdrometer site, and the simulation data are from meridionally (a) 27- and (b) 201-km long arrays of grid boxes and square areas with sizes of (c) 27 km \times 27 km and (d) 201 km \times 201 km centered at the disdrometer site.

the observation (Figures 12a and 12b) are very similar to those obtained from a single grid box that includes the disdrometer site. The Thompson, Thom_aero, and WDM6 schemes show large positive biases, the ISHMAEL scheme shows a relatively small positive bias, the Morrison and P3 schemes show negative biases, and the P3_Nc scheme shows the most dispersive distribution of $\log_{10}M_0$ PDF. The data in the square areas with sizes of 27 km \times 27 km and 201 km \times 201 km also yield almost the same results (Figures 12c and 12d). We also conducted this analysis for other RSD moments and parameters as well and obtained similar findings (not shown). The fact that the simulated RSD characteristics at the site during the analysis period in each simulation are almost identical to those in the other parts of the squall line indicates that the differences in simulated RSD characteristics of this squall line among the seven schemes are very solid. In other words, the spatial uncertainty of the simulations does not have a significant influence on the simulated RSD characteristics, which are primarily determined by the choice of microphysics scheme. The simulated RSD characteristics and their biases for each microphysics scheme also remain almost unchanged when a different planetary boundary layer scheme, a different cumulus scheme, or a different data set for initial and boundary conditions is used (not shown). This indicates that the biases observed in the RSD characteristics in each simulation can actually be attributed to the microphysics scheme used in the simulation.

3.3. Differences in Simulated Cloud Microphysics

The raindrop number concentration at the surface evaluated in the previous subsection is a consequence of physical processes aloft, mainly the cloud microphysical processes. In this subsection, the cloud microphysical reasons behind the biases and discrepancies in N_r prediction in the simulations using different microphysics schemes are examined. Figure 13 shows the time–height diagrams of the rainwater mixing ratio q_r and raindrop number concentration N_r as well as the cloud water mixing ratio q_c and ice mixing ratio q_i (including all ice-phase hydrometeors) above the disdrometer site in the simulations with different microphysics schemes. In a quantitative sense, the simulated q_r is comparable to each other, except for that in the WDM6 simulation: the time-mean rainwater paths in the other six simulations deviate no more than 17% from their average, while that in the WDM6 simulation is 50% larger than the average of the rest. In contrast, there are substantial differences in the simulated

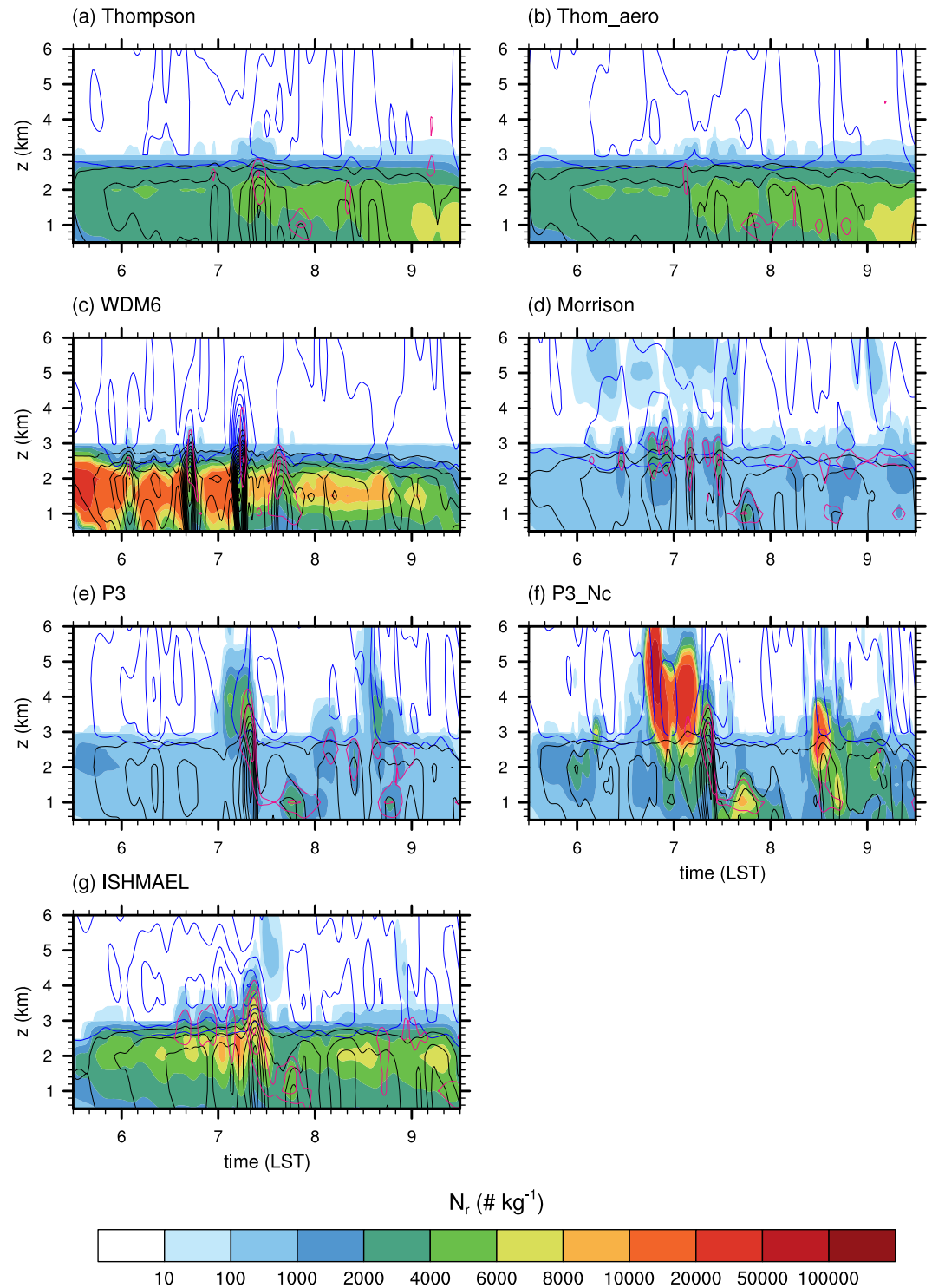


Figure 13. Time–height diagrams of q_r (black contours, in 0.1 g kg^{-1} intervals), q_c (pink contours, in 0.2 g kg^{-1} intervals), q_l (blue contours, in 0.5 g kg^{-1} intervals), and N_r (color shades) at the disdrometer site in the simulations.

N_r . The Thompson and Thom_aero schemes show similar behaviors of N_r , which is quite steady throughout the analysis period and gradually accumulates with time. The WDM6 scheme shows large N_r in the earlier periods and relatively small N_r in the later periods. In this simulation, N_r temporarily decreases when q_r as well as q_c and q_l sharply increases (e.g., 0640–0650 LST; 0710–0720 LST). Note that the periods of sharply increased

hydrometeor mixing ratios with vertically well-developed structures correspond to convective rain periods (see Figure 5c). In the Morrison simulation, N_r is small throughout the entire period, and relatively large N_r appears at the times when q_r increases (e.g., 0640–0700 LST; ~0710 LST) and at the altitudes where relatively large q_c appears at those times ($z \sim 2.0$ – 3.2 km), which is contrary to the behavior of N_r in the WDM6 simulation. The P3 scheme also shows relatively large N_r aloft when q_r sharply increases (0710–0720 LST), up to higher altitudes ($z \sim 4.2$ km) than the Morrison scheme, in consistency with q_c reaching those altitudes. The P3_Nc scheme shows similar behaviors of N_r to the P3 scheme, but large N_r appears up to even higher altitudes and its amount is much larger. Interesting features that the P3 and P3_Nc schemes both show are that there is a less-ice zone (0700–0710 LST for P3 and 0640–0710 LST for P3_Nc, above the melting level) ahead of the most convective part of the system and that the largest N_r appears in this zone and sharply decreases with decreasing altitude. The ISHMAEL scheme also shows relatively large N_r in the convective parts (e.g., 0710–0730 LST), similar to the Morrison, P3, and P3_Nc schemes, but large N_r mainly appears below the melting level and decreases gradually with decreasing altitude, as in the Thompson and Thom_aero simulations.

To summarize the above results, the overall elongation of N_r isolines is close to the horizontal in the Thompson and Thom_aero simulations, close to the vertical in the Morrison, P3, and P3_Nc simulations, and mixed in the WDM6 and ISHMAEL simulations. The horizontal elongation of N_r isolines indicates that stratiform precipitation significantly contributes to N_r , while the vertical elongation indicates that convective precipitation controls N_r . The WDM6 scheme predicts decreases in N_r for convective precipitation, while the Morrison, P3, P3_Nc, and ISHMAEL schemes predict increases in N_r for convective precipitation.

The characteristic behaviors of N_r for each scheme result from the different representations of cloud microphysical processes by the seven schemes. Generally, the autoconversion, melting, raindrop self-collection and collisional breakup (RSCB), and evaporation processes are major microphysical sources and sinks of N_r . Each microphysics scheme has a unique microphysical budget for N_r with different importance of these processes, and a microphysical process that is a very important source/sink for one scheme can be very minor for another scheme. For each of the four microphysical processes, the production/depletion rates of N_r in the simulations with the seven different schemes are compared (Figures 14–17).

The autoconversion process is the process that shows the most dramatic differences in the N_r change rate among the schemes (Figure 14). In terms of this process, the seven schemes can be grouped into three. The Thompson and Thom_aero schemes correspond to the first group, which shows rare occurrences of autoconversion with limited production rates of N_r (the maximum production rates of N_r are in the order of $10^{-2} \text{ kg}^{-1} \text{ s}^{-1}$). Both the schemes employ the autoconversion parameterization of Berry and Reinhardt (1974), which does not give the autoconversion rate when the cloud water mass content is small (H. Lee & Baik, 2017). This explains the rare occurrence of autoconversion. Although the autoconversion occurs rarely, when it occurs, the q_r production rates via autoconversion are not small, unlike the N_r production rates shown in Figures 14a and 14b. The maximum production rates of q_r in the Thompson and Thom_aero simulations are largest among those in the seven simulations except for the P3_Nc simulation (not shown). In many microphysics schemes, the rate of N_r production via autoconversion is parameterized as the q_r production rate divided by the assumed size of produced raindrops. In the Thompson and Thom_aero schemes (since WRF version 4.1), the parameterization of N_r production via autoconversion is designed to produce relatively large raindrops compared to the parameterizations in other schemes most of which are designed to produce raindrops of the smallest size. This makes the N_r production rates in the Thompson and Thom_aero simulations very small. As a result, the contribution of autoconversion to the N_r budget is negligible for these two schemes.

The WDM6 scheme corresponds to the second group, showing no occurrence of autoconversion in Figure 14c. The autoconversion is not totally absent in the simulation, that is, it occurs some distance away from the disdrometer site, but it occurs much more rarely and its rate is much smaller than in the Thompson and Thom_aero simulations. Differently from the description in Lim and Hong (2010), the WDM6 scheme in the WRF model version 4.3.3 uses the autoconversion parameterization of Tripoli and Cotton (1980). In this parameterization, the autoconversion is activated if the cloud water mixing ratio exceeds a certain threshold and the q_r production rate is expressed to be proportional to $q_c^{7/3} N_c^{-1/3}$. The problem is that the current version of WDM6 scheme does not make reasonable predictions of N_c . Although the initial value of N_{CCN} is set to $\sim 10^8 \text{ kg}^{-1}$, it amplifies by several orders, resulting in too large values of N_c . The q_c -weighted mean N_c in the WDM6 simulation is $3.4 \times 10^9 \text{ kg}^{-1}$, which is 17–36 times those in the simulations with the two other schemes that prognose N_c , the

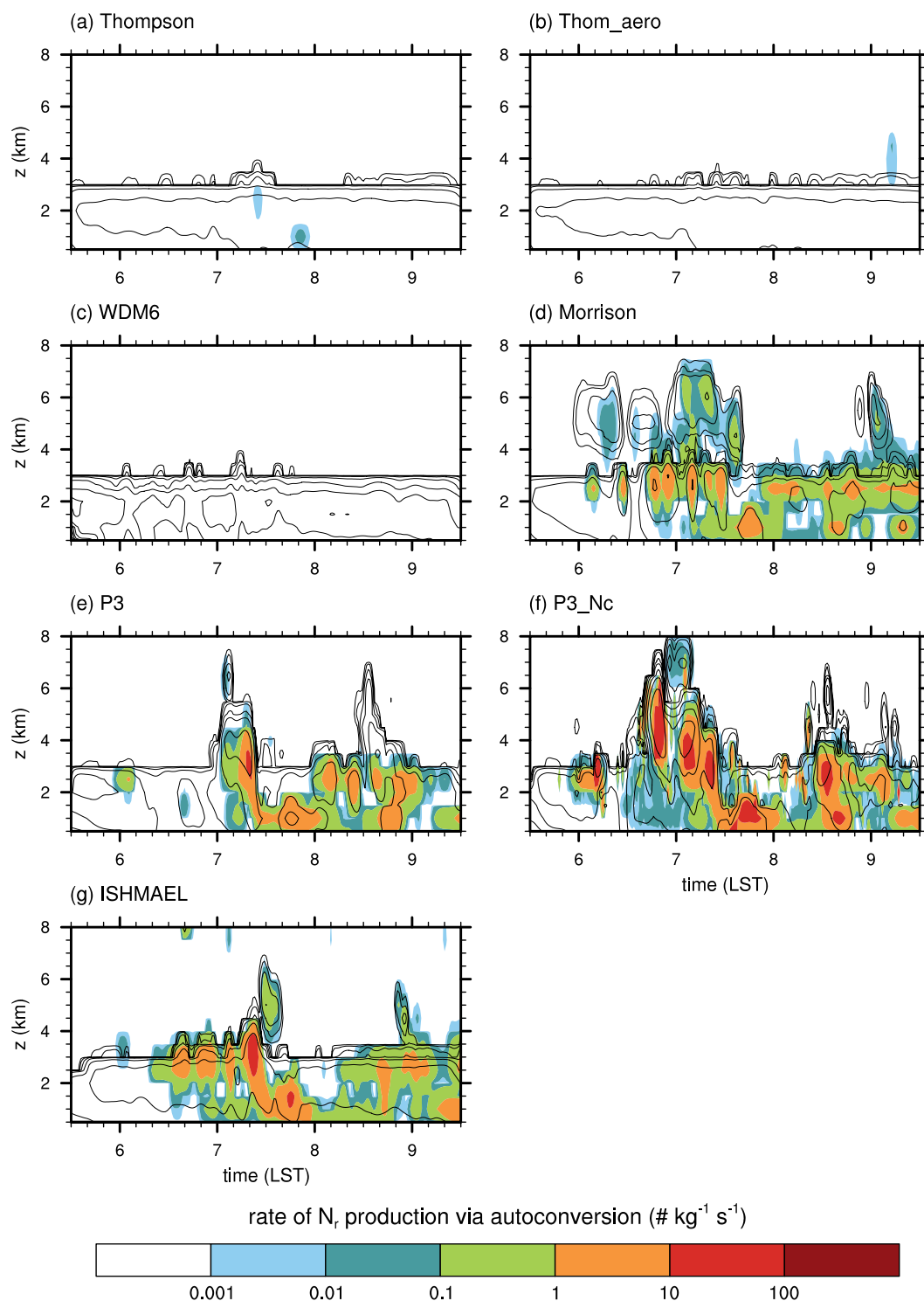


Figure 14. Time–height diagrams of N_r (black contours) and the rate of N_r production via autoconversion (color shades) at the disdrometer site in the simulations. The values for N_r contours are in a geometric sequence with the common ratio of $10^{0.5}$.

Thom_aero ($2.1 \times 10^8 \text{ kg}^{-1}$) and P3_Nc ($9.5 \times 10^7 \text{ kg}^{-1}$) schemes. As a result, the autoconversion is extremely suppressed and it makes no contribution to the N_r budget. In the authors' experience, this issue on N_{CCN} and N_c in the WDM6 scheme has appeared in recent versions of the WRF model, and it explains the contrasting results on the contribution of autoconversion to the N_r budget in the WDM6 scheme between two typhoon case studies of

Wang et al. (2020; WRF version 3.9 is used) and Lin et al. (2022; WRF version 4.2 is used). This issue should be resolved soon. The autoconversion process is known as the key process that causes high raindrop concentration in the convective parts of squall lines (Ferrier et al., 1995; Morrison et al., 2009). The fact that this process is not activated in the convective parts of the system in the WDM6 simulation is responsible for the unrealistic M_3 – M_0 and R – M_0 relationships shown in Section 3.2.

The third group consists of the Morrison, P3, P3_Nc, and ISHMAEL schemes, which show relatively large rates of N_r production via autoconversion (Figures 14d–14g). Those N_r production rates have significant correlations with N_r itself (correlation coefficients being 0.34–0.71), indicating that the autoconversion is an important contributor to the N_r budget in the four schemes. Large N_r production rates appear mostly in the convective parts of the system, at altitudes around the melting level or at low levels ($z < 1.5$ km). Therefore, in the simulations using these four schemes, the active autoconversion in strong convection is the reason for large N_r in the convective parts of the system. To the N_r at the surface, the contribution of the active autoconversion around the melting level seems to be limited because the large number of raindrops produced there sharply decreases while they are falling, presumably via raindrop self-collection. The surface N_r increases mainly when the autoconversion is active at low levels (e.g., 0740–0800 LST). The autoconversion at the low levels is most prominent in the P3_Nc simulation, producing the right peak of the bimodal PDF of $\log_{10} M_0$ at the surface (Figure 7a). The particularly large autoconversion rates in the P3_Nc simulation can be attributed to the prognosis of N_c , which is done only in the P3_Nc scheme among the four schemes in this group. All these four schemes employ the autoconversion parameterization of Khairoutdinov and Kogan (2000), where the autoconversion rate is expressed to be proportional to $q_c^{2.47} N_c^{-1.79}$. Unlike the other schemes where N_c is constant so that it is not depleted by the autoconversion, the P3_Nc scheme reduces N_c as a result of autoconversion, which leads to relatively larger autoconversion rates than those in the other simulations. That the q_c -weighted mean N_c in the P3_Nc simulation ($9.5 \times 10^7 \text{ kg}^{-1}$) is less than half that in the P3 simulation ($2.0 \times 10^8 \text{ kg}^{-1}$) supports this idea. Although allowing depletion of N_c seems to be more reasonable than keeping it constant, the outcome of doing so in the P3_Nc simulation is the appearance of the second mode in the $\log_{10} M_0$ PDF, which corresponds to too large raindrop number concentrations that were never observed. This irony may be caused by the simplicity of the power-law type autoconversion parameterization of Khairoutdinov and Kogan (2000), which results in overestimation of the sensitivity of the autoconversion rate to N_c (H. Lee & Baik, 2017). Among the four schemes, the ISHMAEL scheme shows the weakest correlation between the rate of N_r production via autoconversion and N_r itself (0.34). While the increase in N_r in the convective parts can be well explained by the autoconversion, the stratified pattern of N_r in the stratiform parts is irrelevant with the autoconversion. This implies that microphysical processes other than the autoconversion (e.g., melting and RSCB) are largely responsible for the behavior of N_r in the stratiform parts in the ISHMAEL simulation. The active autoconversion process in the four schemes acts to decrease D_m , especially in the convective parts of the system, as these schemes assume that minimum-sized raindrops are produced via autoconversion. However, those decreases in D_m are often counterbalanced by the accretion of cloud droplets by raindrops, which acts to increase D_m and is also active in the convective parts of the system (not shown).

The melting of ice hydrometeors is another important microphysical source of N_r . All schemes show stratified patterns of the melting rate, but there are large quantitative differences among them (Figure 15). The rate of N_r production via melting is much larger in the Thompson, Thom_aero, WDM6, and ISHMAEL simulations than in the Morrison, P3, and P3_Nc simulations. In the Thompson, Thom_aero, and WDM6 simulations, the rate of N_r production via melting is incomparably larger than that via autoconversion, indicating that the melting process is the dominant source of N_r in these simulations. In the ISHMAEL simulation, the melting process dominates the N_r production in the stratiform parts and overall is the main source of N_r , while it is slightly weakened in the convective parts where the autoconversion also plays an important role. Given that the four schemes all overestimate the surface N_r (Figure 7a) and the melting process is largely responsible for this, there is high possibility that such large rates of N_r production via melting in the four simulations are overestimations. Especially, the WDM6 scheme that most severely overestimates the surface N_r exhibits distinctly larger N_r production rates compared to the other three schemes. The persistence of the large N_r production rates even at altitudes as low as $z = 1$ – 2 km in the WDM6 simulation, which are not seen in any other simulations, leads to the very small surface D_m (Figure 9a). In the Morrison, P3, and P3_Nc simulations, on the other hand, the rates of N_r production via melting and autoconversion are overall comparable, except for the first 1 or 2 hr of the analysis period. For the first hour when the melting is almost the only source of N_r , the three schemes all underestimate the surface N_r (Figure 11). This implies that the N_r production via melting may have been underestimated to some extent in the three simulations.

That the Thompson and WDM6 schemes yield larger rates of N_r production via melting than the Morrison scheme was also shown in a typhoon case study by Lin et al. (2022). However, the melting layer in that case was located at $z = 4\text{--}6$ km so that the influence of the melting process on the surface N_r was very limited due to the active RSCB process below, which made it very difficult to tell which scheme gave more reasonable prediction for the melting process in comparison with the disdrometer data at the surface. The relatively low melting layer ($z \sim 1.5\text{--}3$ km) of the cold-frontal system in the current study to some extent enables the evaluation of melting process prediction using disdrometer data, which raises suspicions that the Thompson and WDM6 schemes produce too many raindrops via melting and the Morrison scheme produces too few raindrops via melting.

For the melting process, the severe disagreements among the schemes shown for the N_r production rate do not occur for the q_r production rate: the coefficient of variation among the schemes is 1.38 for the (temporally and vertically averaged) N_r production rate, about three times that for the q_r production rate (0.49). This indicates that a large portion of the discrepancy in the rate of N_r production via melting among the schemes does not result from the discrepancy in the amount of melting hydrometeors. All seven schemes parameterize the rate of N_r production via melting assuming that the number of melting ice particles is equal to the produced N_r . The number of melting snow particles, for example, is not explicitly computed, but simply calculated as the mass of melting snow divided by the mean particle mass of snow (i.e., the snow mass mixing ratio divided by the snow number concentration). Therefore, the conversion factor N_i/q_i , that is, the ratio of the ice number concentration to the ice mass mixing ratio is critical to the calculation of raindrops produced via melting. This is the point where a large discrepancy among the schemes appears. In the P3, P3_Nc, and ISHMAEL simulations, N_i/q_i averaged over $z = 1.5\text{--}3.0$ km is 1.6×10^6 , 1.5×10^6 , and 1.9×10^7 kg^{-1} , respectively. Even these recently developed schemes that consider flexible evolution of ice particle properties do not agree with each other on this factor, showing approximately one-order differences, mostly due to the discrepancy in the N_i prediction. The average N_i/q_i (calculated for snow and graupel, which are converted to raindrops by melting) in the Morrison simulation (1.0×10^6 kg^{-1}) where N_i is prognosed is close to those in the P3 and P3_Nc simulations, while that in the Thompson (1.6×10^7 kg^{-1}) and Thom_aero (1.7×10^7 kg^{-1}) simulations where N_i is diagnosed is close to that in the ISHMAEL simulation. In the WDM6 simulation where N_i is diagnosed, the average N_i/q_i is two-to-three-order larger (1.6×10^9 kg^{-1}) than those in the other simulations, indicating that the WDM6 scheme diagnoses too many ice particles relative to the ice mass in the melting layer. This amount of N_i/q_i indicates that the mean diameter of raindrops produced via melting is as small as ~ 0.1 mm in the WDM6 simulation, which is unrealistic. The snow and graupel number concentrations in the WDM6 scheme are diagnosed from the mass mixing ratio and temperature based on the aircraft observation study of Houze et al. (1979), and whether the diagnostic relations are valid above 0°C should be carefully checked.

Raindrops produced via autoconversion and melting go through the RSCB process before they reach the surface. Regardless of the scheme, the rate of N_r change via RSCB is well correlated with N_r itself, because this rate is parameterized to be proportional to N_r in all schemes (Beheng, 1994; Cohard & Pinty, 2000; Verlinde & Cotton, 1993) (Figure 16). In the Thompson, Thom_aero, WDM6, and ISHMAEL simulations, the RSCB process substantially decreases N_r throughout the whole analysis period, indicating that the self-collection is always dominant over the collisional breakup. The large amount of N_r mostly produced via melting in these simulations leads to a small mean diameter of raindrops, promoting the active self-collection process. However, raindrops in these simulations do not meet the collection–breakup equilibrium until they reach the surface, which can be seen in the D_m PDFs showing that D_m at the surface in these simulations is much smaller than its equilibrium value (2.1–2.4 mm, depending on the scheme). The ISHMAEL scheme shows much stronger self-collection than the Thompson and Thom_aero schemes, which contributes to the more realistic D_m in the ISHMAEL simulation (Figure 9a). In the Morrison, P3, and P3_Nc simulations, the RSCB process acts as a sink of N_r , especially more in the convective parts, and it sometimes acts as a source of N_r through active collisional breakup when N_r is small. It should be highlighted that the self-collection is dominant over the collisional breakup even in the Morrison and P3 simulations where N_r aloft is already very small. This has led the surface D_m in these simulations to be close to its equilibrium value, which is rarely observed (Figure 9a). Given that the equilibrium value of D_m obtained by numerically solving the stochastic collection and breakup equations is smaller than that prescribed in the Morrison and P3 schemes (Jin et al., 2022; Paukert et al., 2019), lowering the prescribed equilibrium mean raindrop diameter for the RSCB process can be a good modification to these schemes, which will decrease D_m at the surface toward the observed values.

The evaporation process is another microphysical process that raindrops mostly experience before they touch the ground. In all simulations except for the WDM6 simulation, the evaporation process plays a significant role

in the N_r budget at low levels for the first 1 or 2 hr (Figure 17). In these six schemes, the depleted number of raindrops via evaporation is simply calculated as the evaporated mass of rainwater divided by the mean particle mass of raindrops (q_r/N_r). Therefore, the rate of N_r depletion via evaporation is overall larger in the Thompson, Thom_aero, and ISHMAEL simulations than in the Morrison and P3 simulations, because of the overall larger N_r . In the P3_Nc simulation, the evaporation contributes to reducing the numerous raindrops produced via autoconversion above $z \sim 3$ km. Note that the method used to calculate the N_r depletion via evaporation in the six schemes conserves the mean volume diameter of raindrops (also D_m if μ is constant) during evaporation, which is only reasonable under very specific conditions as the mean raindrop diameter almost always decreases during evaporation (Seifert, 2008). Unlike in the other simulations, in the WDM6 simulation, the evaporation process has almost no influence on N_r , except for the earliest times in the analysis period. This is attributed to the different method used to represent the depletion of raindrop number via evaporation in the WDM6 scheme, that is, completely depleting N_r at once only when either q_r is completely depleted via evaporation or the mean volume diameter of raindrops becomes smaller than $82 \mu\text{m}$. The evaporation does not affect N_r at all unless this condition is satisfied. Therefore, in the WDM6 simulation, as long as the precipitation reaches the surface, no raindrops completely evaporate regardless of the relative humidity of environment. This method is certainly problematic, and it must have contributed to the overestimation of N_r at the surface in the WDM6 simulation.

4. Summary and Conclusions

In this study, we evaluated the raindrop number concentration predictions of seven different double-moment microphysics schemes in squall-line case simulations in comparison with ground-based disdrometer observations. In contrast to the M_3 (rainwater mass) prediction on which the microphysics schemes agree with each other, the M_0 (raindrop number) predictions of the seven schemes show severe discrepancies among the schemes and significant biases from the observation. In other words, the double-moment microphysics schemes do not make reliable predictions on the raindrop number concentration. The biases in the raindrop number concentration prediction lead to the biases in the predictions of high-order RSD moments, D_m , and N_w , which highlights the importance of accurate raindrop number concentration prediction. The simulations show significant changes in the relationship between the raindrop number and rainwater mass within the rainfall event, which are not seen in the observation. The evaluation of the raindrop number concentration prediction of each microphysics scheme is summarized as follows:

- The Thompson and Thom_aero schemes substantially overestimate N_r . The main source of N_r in these schemes is melting of snow and graupel, which implies that the number of melting ice particles may be overestimated.
- The WDM6 scheme shows the most severe overestimation of N_r , which originates from the unrealistically large number of ice particles in the melting layer diagnosed in this scheme. This scheme shows an unrealistic behavior of N_r , that is, temporary decreases in N_r in opposition to the increases in q_r in the convective parts of the squall line, as it fails to reproduce active raindrop production via autoconversion in those parts.
- The Morrison and P3 schemes show negatively biased distribution of N_r . The contributions of autoconversion and melting to N_r production are comparable in these schemes. It is expected that the negative biases of N_r would be alleviated if the prescribed equilibrium mean raindrop diameter for the RSCB process is lowered.
- The P3_Nc scheme shows two prominent modes in N_r distribution, one of which is negatively biased and the other of which is substantially positively biased from the observed mode. The latter is associated with overly active autoconversion in the convective parts of the squall line, which may be caused by the use of simple power-law type autoconversion parameterization coupled with the prognosis of cloud droplet number concentration in this scheme.
- The ISHMAEL scheme overestimates N_r but not as much as the Thompson, Thom_aero, and WDM6 schemes, showing the most realistic predictions of M_0 , D_m , and N_w . In this scheme, melting plays the most important role in N_r production in the stratiform parts of the squall line, while autoconversion takes the role in the convective parts.

That the severe discrepancies among the microphysics schemes and thus the high uncertainty in the prediction of N_r originate from the different representations of specific microphysical processes among the schemes implies that this high uncertainty can be reduced by careful selections of parameterizations for the microphysical processes. The biases in N_r prediction and their microphysical reasons examined in this study for a variety of double-moment microphysics schemes may be considered in the future updates of these schemes or in the development of a new scheme.

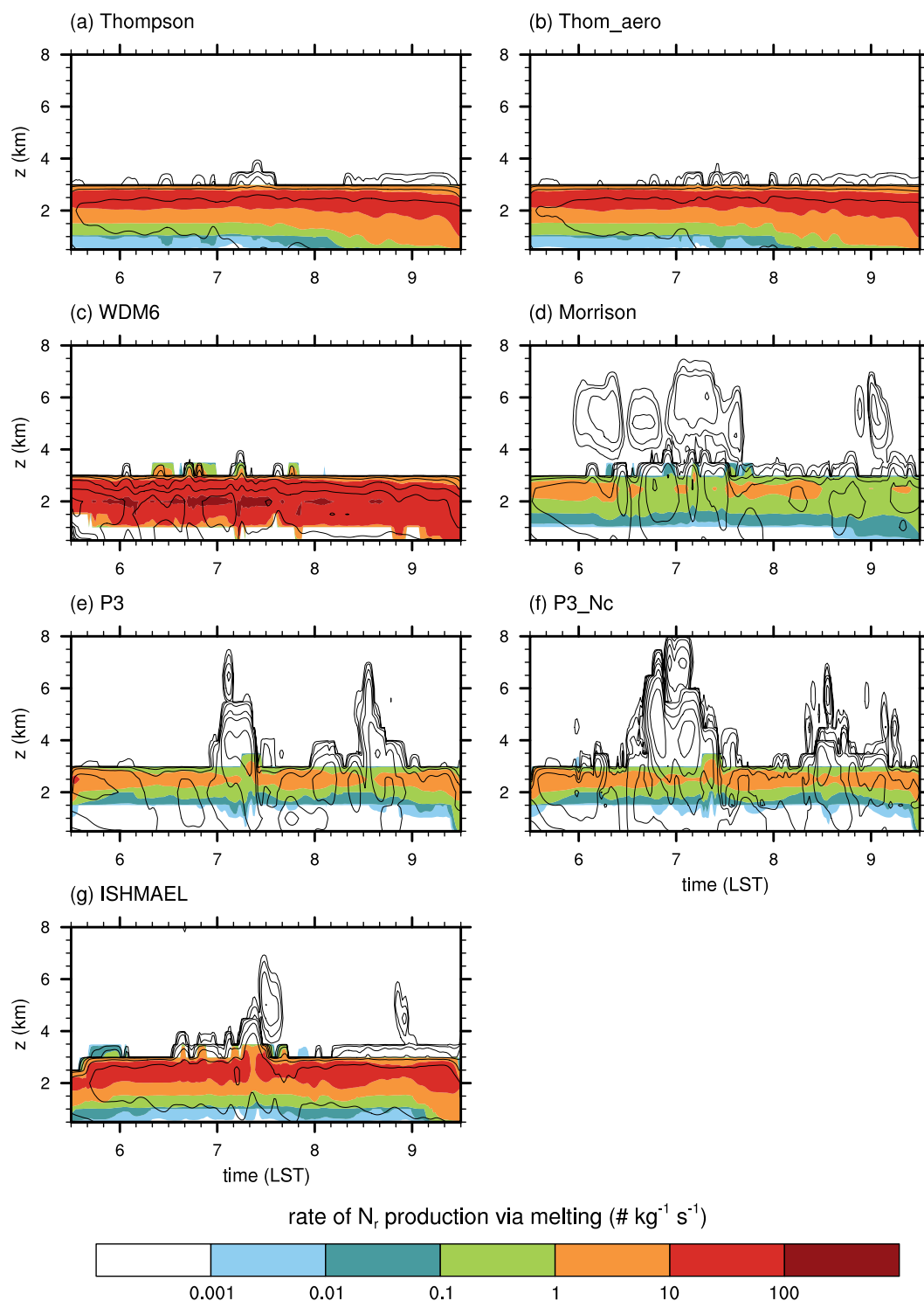


Figure 15. As in Figure 14, but for the rate of N_r production via melting.

Double-moment microphysics schemes have been built with an aim to benefit from the prediction of hydrometeor particle number concentration, but not much effort has been made to predict the number concentration accurately. This is shown from the fact that the N_r change rates for autoconversion, melting, and evaporation in most schemes are not parameterized explicitly but are simply parameterized to be proportional to the corresponding q_r change rates. The conversion factors used to convert the q_r change rates to the N_r change rates are mostly arbitrary, acting

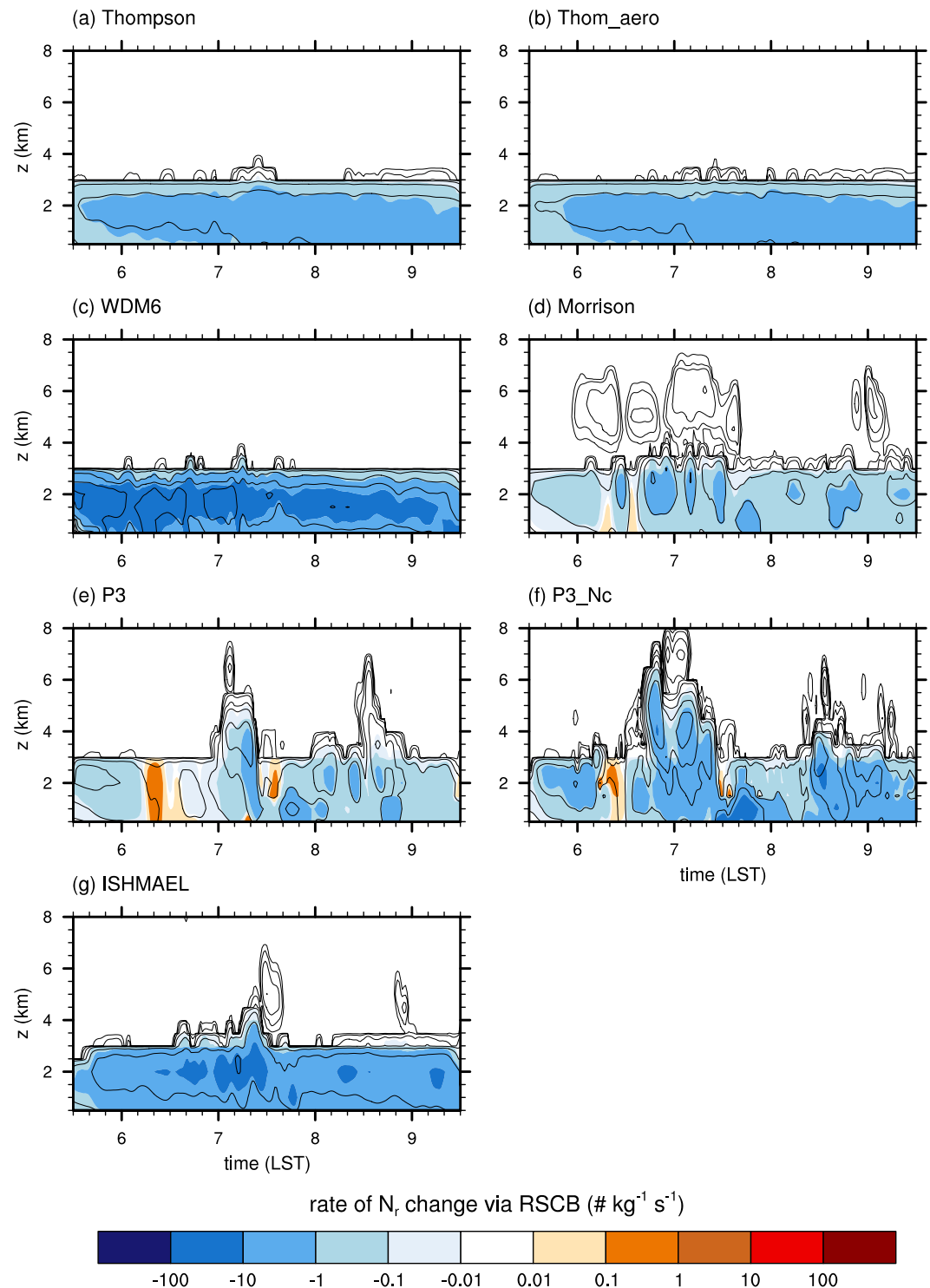


Figure 16. As in Figure 14, but for the rate of N_r change via raindrop self-collection and collisional breakup.

as significant sources of the uncertainty in N_r prediction. This encourages development of explicit parameterizations for the N_r change rates based on the governing equation of each microphysical process, which have the potential to reduce the uncertainty in N_r prediction and be widely applicable. For example, the autoconversion parameterization of H. Lee and Baik (2017) was developed based on the quasi-stochastic collection equation where a sophisticated approximation of collision efficiency is included. This parameterization explicitly represents the

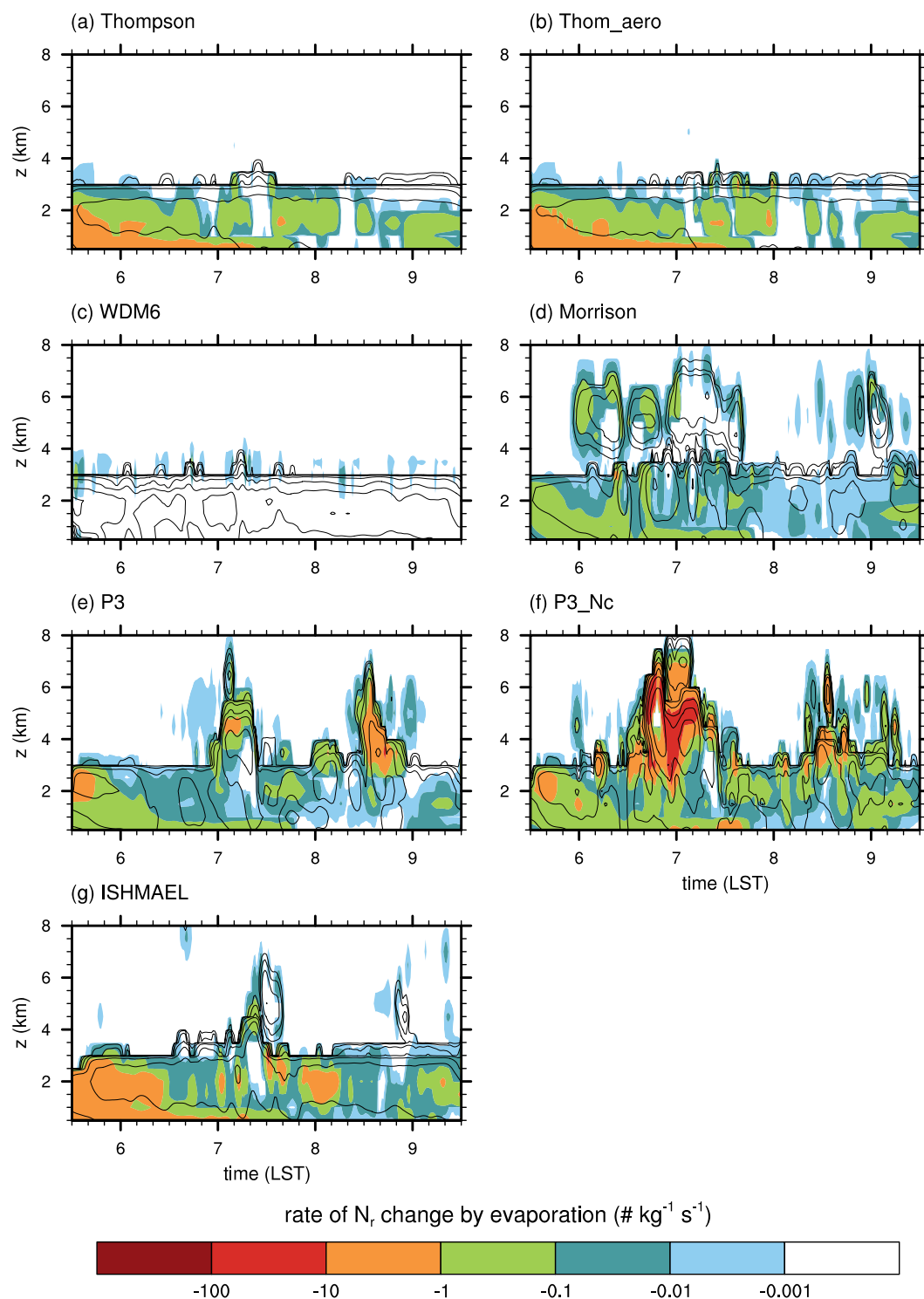


Figure 17. As in Figure 14, but for the rate of N_r change via evaporation.

N_r production rate via autoconversion, apart from the q_r production rate, which can reduce the uncertainty in N_r prediction. Meanwhile, for some microphysical processes (e.g., the drop shedding from ice particles), reliable governing equations are currently unavailable because of the imperfect understanding of cloud microphysics at the process level. New laboratory experiments, in-situ observations, and direct numerical simulations for those processes are required to better understand the processes and thus to improve their parameterizations.

Data Availability Statement

The disdrometer data and WRF model simulation outputs used in this study are archived in Mendeley Data (Jin, 2022). The ERA5 data can be downloaded from the Copernicus Climate Change Service (C3S) Climate Data Store (CDS, 2018a, 2018b). The multi-radar composite data and automatic weather station data provided by the Korea Meteorological Administration can be downloaded from <https://data.kma.go.kr/data/grnd/selectAwsRltm-List.do?pgmNo=56> and <https://data.kma.go.kr/data/rmt/rmtList.do?code=11&pgmNo=62>, respectively.

Acknowledgments

The authors are grateful to three anonymous reviewers who provided valuable comments that helped improve this paper. This work was supported by the National Research Foundation of Korea under Grant 2021R1A2C1007044.

References

- Atlas, D., Srivastava, R. C., & Sekhon, R. S. (1973). Doppler radar characteristics of precipitation at vertical incidence. *Reviews of Geophysics*, 11, 1–35. <https://doi.org/10.1029/rg01i001p00001>
- Beheng, K. D. (1994). A parameterization of warm cloud microphysical conversion processes. *Atmospheric Research*, 33(1–4), 193–206. [https://doi.org/10.1016/0169-8095\(94\)90020-5](https://doi.org/10.1016/0169-8095(94)90020-5)
- Berry, E. X., & Reinhardt, R. L. (1974). An analysis of cloud drop growth by collection: Part II. Single initial distributions. *Journal of the Atmospheric Sciences*, 31(7), 1825–1831. [https://doi.org/10.1175/1520-0469\(1974\)031<1825:aaocdg>2.0.co;2](https://doi.org/10.1175/1520-0469(1974)031<1825:aaocdg>2.0.co;2)
- Bringi, V. N., Chandrasekar, V., Hubbert, J., Gorgucci, E., Randeu, W. L., & Schoenhuber, M. (2003). Raindrop size distribution in different climatic regimes from disdrometer and dual-polarized radar analysis. *Journal of the Atmospheric Sciences*, 60(2), 354–365. [https://doi.org/10.1175/1520-0469\(2003\)060<0354:rsdidi>2.0.co;2](https://doi.org/10.1175/1520-0469(2003)060<0354:rsdidi>2.0.co;2)
- Brown, B. R., Bell, M. M., & Frambach, A. J. (2016). Validation of simulated hurricane drop size distributions using polarimetric radar. *Geophysical Research Letters*, 43(2), 910–917. <https://doi.org/10.1002/2015gl067278>
- Cao, Q., Zhang, G., Brandes, E., Schuur, T., Ryzhkov, A., & Ikeda, K. (2008). Analysis of video disdrometer and polarimetric radar data to characterize rain microphysics in Oklahoma. *Journal of Applied Meteorology and Climatology*, 47(8), 2238–2255. <https://doi.org/10.1175/2008jame1732.1>
- CDS. (2018a). ERA5 hourly data on pressure levels from 1940 to present [Dataset]. Copernicus Climate Change Service (C3S) Climate Data Store (CDS). <https://doi.org/10.24381/cds.bd0915c6>
- CDS. (2018b). ERA5 hourly data on single levels from 1940 to present [Dataset]. Copernicus Climate Change Service (C3S) Climate Data Store (CDS). <https://doi.org/10.24381/cds.adbb2d47>
- Chen, G., Zhao, K., Huang, H., Yang, Z., Lu, Y., & Yang, J. (2021). Evaluating simulated raindrop size distributions and ice microphysical processes with polarimetric radar observations in a Meiyu front event over Eastern China. *Journal of Geophysical Research: Atmospheres*, 126(22), e2020JD034511. <https://doi.org/10.1029/2020jd034511>
- Cohard, J. M., & Pinty, J. P. (2000). A comprehensive two-moment warm microphysical bulk scheme. I: Description and tests. *Quarterly Journal of the Royal Meteorological Society*, 126(566), 1815–1842. <https://doi.org/10.1002/qj.49712656613>
- Colarco, P., da Silva, A., Chin, M., & Diehl, T. (2010). Online simulations of global aerosol distributions in the NASA GEOS-4 model and comparisons to satellite and ground-based aerosol optical depth. *Journal of Geophysical Research*, 115(D14), D14207. <https://doi.org/10.1029/2009jd012820>
- Ferrier, B. S., Tao, W.-K., & Simpson, J. (1995). A double-moment multiple-phase four-class bulk ice scheme. Part II: Simulations of convective storms in different large-scale environments and comparisons with other bulk parameterizations. *Journal of the Atmospheric Sciences*, 52(8), 1001–1033. [https://doi.org/10.1175/1520-0469\(1995\)052<1001:admmpf>2.0.co;2](https://doi.org/10.1175/1520-0469(1995)052<1001:admmpf>2.0.co;2)
- Hersbach, H., Bell, B., Berrisford, P., Hirahara, S., Horányi, A., Muñoz-Sabater, J., et al. (2020). The ERA5 global reanalysis. *Quarterly Journal of the Royal Meteorological Society*, 146(730), 1999–2049. <https://doi.org/10.1002/qj.3803>
- Hong, S.-Y., & Lim, J.-O. J. (2006). The WRF single-moment 6-class microphysics scheme (WSM6). *Journal of the Korean Meteorological Society*, 42, 129–151.
- Hong, S.-Y., Noh, Y., & Dudhia, J. (2006). A new vertical diffusion package with an explicit treatment of entrainment processes. *Monthly Weather Review*, 134(9), 2318–2341. <https://doi.org/10.1175/mwr3199.1>
- Houze, R. A., Jr., Hobbs, P. V., Herzegh, P. H., & Parsons, D. B. (1979). Size distributions of precipitation particles in frontal clouds. *Journal of the Atmospheric Sciences*, 36(1), 156–162. [https://doi.org/10.1175/1520-0469\(1979\)036<0156:sdoppi>2.0.co;2](https://doi.org/10.1175/1520-0469(1979)036<0156:sdoppi>2.0.co;2)
- Iacono, M. J., Delamere, J. S., Mlawer, E. J., Shephard, M. W., Clough, S. A., & Collins, W. D. (2008). Radiative forcing by long-lived greenhouse gases: Calculations with the AER radiative transfer models. *Journal of Geophysical Research*, 113(D13), D13103. <https://doi.org/10.1029/2008jd009944>
- Igel, A. L., Igel, M. R., & van den Heever, S. C. (2015). Make it a double? Sobering results from simulations using single-moment microphysics schemes. *Journal of the Atmospheric Sciences*, 72(2), 910–925. <https://doi.org/10.1175/jas-d-14-0107.1>
- Jaffrain, J., & Berne, A. (2011). Experimental quantification of the sampling uncertainty associated with measurements from PARSIVEL disdrometers. *Journal of Hydrometeorology*, 12(3), 352–370. <https://doi.org/10.1175/2010jhm1244.1>
- Jensen, A. A., Harrington, J. Y., Morrison, H., & Milbrandt, J. A. (2017). Predicting ice shape evolution in a bulk microphysics model. *Journal of the Atmospheric Sciences*, 74(6), 2081–2104. <https://doi.org/10.1175/jas-d-16-0350.1>
- Jiménez, P. A., Dudhia, J., González-Rouco, J. F., Navarro, J., Montávez, J. P., & García-Bustamante, E. (2012). A revised scheme for the WRF surface layer formulation. *Monthly Weather Review*, 140(3), 898–918. <https://doi.org/10.1175/mwr-d-11-00056.1>
- Jin, H.-G. (2022). Disdrometer and WRF model output data for “Do double-moment microphysics schemes make reliable predictions on the raindrop number concentration?: A squall-line case study” [Dataset]. Mendeley Data. <https://doi.org/10.17632/spwdznjnk2.1>
- Jin, H.-G., Baik, J.-J., Lee, H., & Ahmed, T. (2022). A new warm-cloud collection and breakup parameterization scheme for weather and climate models. *Atmospheric Research*, 272, 106145. <https://doi.org/10.1016/j.atmosres.2022.106145>
- Jwa, M., Jin, H.-G., Lee, J., Moon, S., & Baik, J.-J. (2021). Characteristics of raindrop size distribution in Seoul, South Korea according to rain and weather types. *Asia-Pacific Journal of Atmospheric Sciences*, 57(3), 605–617. <https://doi.org/10.1007/s13143-020-00219-w>
- Kain, J. S. (2004). The Kain–Fritsch convective parameterization: An update. *Journal of Applied Meteorology*, 43(1), 170–181. [https://doi.org/10.1175/1520-0450\(2004\)043<0170:tkcpau>2.0.co;2](https://doi.org/10.1175/1520-0450(2004)043<0170:tkcpau>2.0.co;2)
- Khairoutdinov, M., & Kogan, Y. (2000). A new cloud physics parameterization in a large-eddy simulation model of marine stratocumulus. *Monthly Weather Review*, 128(1), 229–243. [https://doi.org/10.1175/1520-0493\(2000\)128<0229:ancppi>2.0.co;2](https://doi.org/10.1175/1520-0493(2000)128<0229:ancppi>2.0.co;2)
- Lee, H., & Baik, J.-J. (2017). A physically based autoconversion parameterization. *Journal of the Atmospheric Sciences*, 74(5), 1599–1616. <https://doi.org/10.1175/jas-d-16-0207.1>

- Lee, J., Jin, H.-G., & Baik, J.-J. (2022). Regional differences in raindrop size distribution observed from disdrometers in South Korea and their possible causes. *Theoretical and Applied Climatology*, 150(1–2), 847–862. <https://doi.org/10.1007/s00704-022-04192-4>
- Lei, H., Guo, J., Chen, D., & Yang, J. (2020). Systematic bias in the prediction of warm-rain hydrometeors in the WDM6 microphysics scheme and modifications. *Journal of Geophysical Research: Atmospheres*, 125(4), e2019JD030756. <https://doi.org/10.1029/2019jd030756>
- Lim, K.-S. S., & Hong, S.-Y. (2010). Development of an effective double-moment cloud microphysics scheme with prognostic cloud condensation nuclei (CCN) for weather and climate models. *Monthly Weather Review*, 138(5), 1587–1612. <https://doi.org/10.1175/2009mwr2968.1>
- Lin, L., Yuan, H., Bao, X., Chen, W., Zhang, S., & Xu, F. (2022). Evaluation of the raindrop size distribution representation of microphysics schemes in Typhoon Lekima using disdrometer network observations. *Atmospheric Research*, 278, 106346. <https://doi.org/10.1016/j.atmosres.2022.106346>
- Lynn, B. H., Khain, A. P., Dudhia, J., Rosenfeld, D., Pokrovsky, A., & Seifert, A. (2005). Spectral (bin) microphysics coupled with a mesoscale model (MM5). Part I: Model description and first results. *Monthly Weather Review*, 133(1), 44–58. <https://doi.org/10.1175/mwr-2840.1>
- Milbrandt, J. A., & McTaggart-Cowan, R. (2010). Sedimentation-induced errors in bulk microphysics schemes. *Journal of the Atmospheric Sciences*, 67(12), 3931–3948. <https://doi.org/10.1175/2010jas3541.1>
- Morrison, H., Curry, J. A., & Khvorostyanov, V. I. (2005). A new double-moment microphysics parameterization for application in cloud and climate models. Part I: Description. *Journal of the Atmospheric Sciences*, 62(6), 1665–1677. <https://doi.org/10.1175/jas3446.1>
- Morrison, H., Kumjian, M. R., Martinkus, C. P., Prat, O. P., & van Lier-Walqui, M. (2019). A general N -moment normalization method for deriving raindrop size distribution scaling relationships. *Journal of Applied Meteorology and Climatology*, 58(2), 247–267. <https://doi.org/10.1175/jamc-d-18-0060.1>
- Morrison, H., Lawson, P., & Chandrakar, K. K. (2022). Observed and bin model simulated evolution of drop size distributions in high-based cumulus congestus over the United Arab Emirates. *Journal of Geophysical Research: Atmospheres*, 127(3), e2021JD035711. <https://doi.org/10.1029/2021jd035711>
- Morrison, H., & Milbrandt, J. A. (2015). Parameterization of cloud microphysics based on the prediction of bulk ice particle properties. Part I: Scheme description and idealized tests. *Journal of the Atmospheric Sciences*, 72(1), 287–311. <https://doi.org/10.1175/jas-d-14-0065.1>
- Morrison, H., Milbrandt, J. A., Bryan, G. H., Ikeda, K., Tessoroff, S. A., & Thompson, G. (2015). Parameterization of cloud microphysics based on the prediction of bulk ice particle properties. Part II: Case study comparisons with observations and other schemes. *Journal of the Atmospheric Sciences*, 72(1), 312–339. <https://doi.org/10.1175/jas-d-14-0066.1>
- Morrison, H., Thompson, G., & Tatarskii, V. (2009). Impacts of cloud microphysics on the development of trailing stratiform precipitation in a simulated squall line: Comparison of one- and two-moment schemes. *Monthly Weather Review*, 137(3), 991–1007. <https://doi.org/10.1175/2008mwr2556.1>
- Morrison, H., van Lier-Walqui, M., Fridlind, A. M., Grabowski, W. W., Harrington, J. Y., Hoose, C., et al. (2020). Confronting the challenge of modeling cloud and precipitation microphysics. *Journal of Advances in Modeling Earth Systems*, 12, e2019MS001689. <https://doi.org/10.1029/2019MS001689>
- Paukert, M., Fan, J., Rasch, P. J., Morrison, H., Milbrandt, J. A., Shpund, J., & Khain, A. (2019). Three-moment representation of rain in a bulk microphysics model. *Journal of Advances in Modeling Earth Systems*, 11(1), 257–277. <https://doi.org/10.1029/2018ms001512>
- Rutledge, S. A., & Hobbs, P. V. (1983). The mesoscale and microscale structure and organization of clouds and precipitation in midlatitude cyclones. VIII: A model for the “seeder-feeder” process in warm-frontal rainbands. *Journal of the Atmospheric Sciences*, 40(5), 1185–1206. [https://doi.org/10.1175/1520-0469\(1983\)040<1185:tmamsa>2.0.co;2](https://doi.org/10.1175/1520-0469(1983)040<1185:tmamsa>2.0.co;2)
- Seifert, A. (2008). On the parameterization of evaporation of raindrops as simulated by a one-dimensional rainshaft model. *Journal of the Atmospheric Sciences*, 65(11), 3608–3619. <https://doi.org/10.1175/2008jas2586.1>
- Seifert, A., & Beheng, K. D. (2001). A double-moment parameterization for simulating autoconversion, accretion and selfcollection. *Atmospheric Research*, 59, 265–281. [https://doi.org/10.1016/s0169-8095\(01\)00126-0](https://doi.org/10.1016/s0169-8095(01)00126-0)
- Skamarock, W. C., Klemp, J. B., Dudhia, J., Gill, D. O., Liu, Z., Berner, J., et al. (2019). A description of the Advanced Research WRF model version 4. In *NCAR technical notes NCAR/TN-556+STR*. National Center for Atmospheric Research.
- Testud, J., Oury, S., Black, R. A., Amayenc, P., & Dou, X. (2001). The concept of “normalized” distribution to describe raindrop spectra: A tool for cloud physics and cloud remote sensing. *Journal of Applied Meteorology*, 40(6), 1118–1140. [https://doi.org/10.1175/1520-0450\(2001\)040<1118:tcondt>2.0.co;2](https://doi.org/10.1175/1520-0450(2001)040<1118:tcondt>2.0.co;2)
- Tewari, M., Chen, F., Wang, W., Dudhia, J., LeMone, M. A., Mitchell, K., et al. (2004). Implementation and verification of the unified Noah land surface model in the WRF model. In *Paper presented at 20th conference on weather analysis and forecasting/16th conference on numerical weather prediction*. American Meteorological Society.
- Thompson, E. J., Rutledge, S. A., Dolan, B., & Thurai, M. (2015). Drop size distributions and radar observations of convective and stratiform rain over the equatorial Indian and west Pacific Oceans. *Journal of the Atmospheric Sciences*, 72(11), 4091–4125. <https://doi.org/10.1175/jas-d-14-0206.1>
- Thompson, G., & Eidhammer, T. (2014). A study of aerosol impacts on clouds and precipitation development in a large winter cyclone. *Journal of the Atmospheric Sciences*, 71(10), 3636–3658. <https://doi.org/10.1175/jas-d-13-0305.1>
- Thompson, G., Field, P. R., Rasmussen, R. M., & Hall, W. D. (2008). Explicit forecasts of winter precipitation using an improved bulk microphysics scheme. Part II: Implementation of a new snow parameterization. *Monthly Weather Review*, 136(12), 5095–5115. <https://doi.org/10.1175/2008mwr2387.1>
- Tokay, A., Wolff, D. B., & Petersen, W. A. (2014). Evaluation of the new version of the laser-optical disdrometer, OTT Parsivel². *Journal of Atmospheric and Oceanic Technology*, 31(6), 1276–1288. <https://doi.org/10.1175/jtech-d-13-00174.1>
- Tripoli, G. J., & Cotton, W. R. (1980). A numerical investigation of several factors contributing to the observed variable intensity of deep convection over South Florida. *Journal of Applied Meteorology and Climatology*, 19(9), 1037–1063. [https://doi.org/10.1175/1520-0450\(1980\)019<1037:aniosf>2.0.co;2](https://doi.org/10.1175/1520-0450(1980)019<1037:aniosf>2.0.co;2)
- Verlinde, J., & Cotton, W. R. (1993). Fitting microphysical observations of nonsteady convective clouds to a numerical model: An application of the adjoint technique of data assimilation to a kinematic model. *Monthly Weather Review*, 121(10), 2776–2793. [https://doi.org/10.1175/1520-0493\(1993\)121<2776:fmoonc>2.0.co;2](https://doi.org/10.1175/1520-0493(1993)121<2776:fmoonc>2.0.co;2)
- Wang, M., Zhao, K., Pan, Y., & Xue, M. (2020). Evaluation of simulated drop size distributions and microphysical processes using polarimetric radar observations for landfalling Typhoon Matmo (2014). *Journal of Geophysical Research: Atmospheres*, 125(6), e2019JD031527. <https://doi.org/10.1029/2019jd031527>

- Witte, M. K., Chuang, P. Y., Ayala, O., Wang, L.-P., & Feingold, G. (2019). Comparison of observed and simulated drop size distributions from large-eddy simulations with bin microphysics. *Monthly Weather Review*, *147*(2), 477–493. <https://doi.org/10.1175/mwr-d-18-0242.1>
- Wu, D., Zhang, F., Chen, X., Ryzhkov, A., Zhao, K., Kumjian, M. R., et al. (2021). Evaluation of microphysics schemes in tropical cyclones using polarimetric radar observations: Convective precipitation in an outer rainband. *Monthly Weather Review*, *149*(4), 1055–1068. <https://doi.org/10.1175/mwr-d-19-0378.1>